

# Supplementary Information

## A Fully Integrated Smart Ring for Daily Biochemical Monitoring

Tamoghna Saha<sup>a\*</sup>, Shichao Ding<sup>a\*</sup>, Siyu Qin<sup>b\*</sup>, Hannah Fishman<sup>a</sup>, Rosie Pham<sup>c</sup>, Te Gu<sup>a</sup>,  
Muyang Lin<sup>a</sup>, Yushan Xian<sup>b</sup>, Barak Sabbagh<sup>a</sup>, Abdulhameed Abdal<sup>d</sup>, Gaoyuan Ji<sup>b</sup>, Kittiya  
Sakdaphetsiri<sup>a</sup> Muhammad Inam Khan<sup>a</sup>, Hao Luan<sup>a</sup>, Omeed Djasemmi<sup>b</sup>, Samar Singh  
Sandhu<sup>a</sup>, Sheng Xu<sup>a</sup>, Joseph Wang<sup>a#</sup>

<sup>a</sup> Aiso Yufeng Li Family Department of Chemical and Nanoengineering, University of  
California San Diego, La Jolla, CA 92093, USA

<sup>b</sup> Department of Electrical and Computer Engineering, University of California San Diego,  
La Jolla, CA 92093, USA

<sup>c</sup> Department of Bioengineering, University of California San Diego, La Jolla, CA 92093,  
USA

<sup>d</sup> Department of Mechanical Engineering, University of California San Diego, La Jolla, CA  
92161, USA

<sup>§</sup> Equal Contribution

\* Corresponding Author: [josephwang@ucsd.edu](mailto:josephwang@ucsd.edu)

29  
30  
31  
32  
33  
34  
35  
36  
37  
38  
39  
40  
41  
42  
43  
44  
45  
46  
47  
48  
49  
50  
51  
52  
53  
54  
55  
56

## Table of Contents

- Figure.S1:** CHARM assembling process.
- Figure.S2:** Optical image of the fluidic channel showing liquid advancement at 150 nl/min flow rate.
- Supplementary Note 1:** Theoretical estimation of hydrogel osmotic pressure
- Figure.S3:**  $G'/G''$  vs. strain rate plot of hydrogels at angular frequency of 10 rad/s.
- Figure.S4:** Optical image of the fluidic channel showing greater dye penetration due to osmosis vs. natural perspiration.
- Supplementary Note 2:** Von Mises stress estimation on hydrogel surface
- Figure.S5:** Mechanical simulation of the hydrogel under bending.
- Figure.S6:** In-vitro performance of the glucose sensor.
- Figure.S7:** In-vitro performance of the ascorbic acid sensor.
- Figure.S8:** In-vitro performance of the uric acid sensor.
- Figure.S9:** In-vitro performance of the ketone sensor.
- Figure.S10:** In-vitro performance of the lactate sensor.
- Figure.S11:** In-vitro performance of the alcohol sensor.
- Supplementary Note 3: Numerical simulation of analyte flux under varying concentrations and sweat rates**
- Figure.S12:** Schematic illustration and mathematical formulation of the fluid flow numerical model.
- Figure.S13:** Mesh Convergence and Numerical Validation.
- Figure.S14:** Transient numerical simulation showing time-dependent inlet concentration changes.
- Supplementary Note 4.** Electronic system overview and control architecture.
- Supplementary Note 5.** Debug and deployment configurations.
- Supplementary Note 6.** Power consumption measurement methodology 1.
- Supplementary Note 7.** Power consumption measurement methodology 2.
- Supplementary Note 8.** Power consumption measurement methodology 3.

57 **Figure.S15:** Circuit schematics.

58 **Figure.S16:** F-PCB layer and drill layout.

59 **Figure.S17:** Bill of materials.

60 **Figure.S18:** Low-power control flow chart.

61 **Figure.S19:** Chronoamperometric response from 4 channels in the F-PCB, operating  
62 sequentially for peroxide detection in a Prussian blue-carbon electrode system.

63 **Figure.S20:** Chronoamperometric response from 4 channels in the F-PCB, operating  
64 sequentially for glucose, VC, UA, and BHB detection at their respective potentials.

65 **Figure.S21:** Optical images of the layer-by-layer printing of the flexible AgO-Zn battery.

66 **Figure.S22:** SEM images of the current collectors and layers of the AgO-Zn battery.

67 **Figure.S23:** SEM images of the different layers of the flexible AgO-Zn battery after  
68 bending.

69 **Figure.S24:** The voltage-capacity plot of in-series batteries with varying charging-  
70 discharging rates.

71 **Figure.S25:** The voltage-capacity plot of the battery under 0.5 C-rate.

72 **Figure.S26:** The voltage-capacity plot of the battery under bending.

73 **Supplementary Note 9:** Calibration model to acquire blood concentration dynamics from  
74 sensor's  $I(t)$

75 **Figure.S27:** Flow chart of personalized calibration protocol for glucose.

76 **Figure.S28:** Glucose profile of T1D subject over multiple days.

77 **Figure.S29:** Ketone profile of T1D subject over multiple days.

78 **Figure.S30:** Utilization of the personalized calibration protocol to convert current to  
79 concentration in a daily test.

80 **Figure.S31:** Current profiles of glucose and ketone related to Figure.5a i and ii.

81 **Figure.S32:** Lactate profile of T1D subject over multiple days.

82 **Figure.S33:** Alcohol profile of T1D subject over multiple days.

83 **Figure.S34:** Current profiles of glucose and ketone related to Figure.5b.

84 **Figure.S35:** Current profiles of glucose, BHB, alcohol and lactate from T1D subject  
85 related to Fig.5c.

86 **Figure.S36:** UA (blue) and VC (green) profile of T1D subject over multiple days.  
87 **Figure.S37:** Glucose profile of healthy subject over multiple days.  
88 **Figure.S38:** BHB profile of healthy subject over multiple days.  
89 **Figure.S39:** UA profile of healthy subject over multiple days.  
90 **Figure.S40:** Lactate profile of healthy subject over multiple days.  
91 **Figure.S41:** Alcohol profile of healthy subject over multiple days.  
92 **Figure.S42:** Current profiles of glucose, AA, UA and BHB from T1D subject related to  
93 Fig.6a.  
94 **Figure.S43:** Current profiles of glucose, BHB, alcohol and lactate from the healthy subject  
95 related to Figure.6a.  
96 **Figure.S44:** Comparison of MARD vs. Rate of *SBG* (*t*) change.  
97 **Figure.S45:** Cytotoxicity test of CHARM's components.

98

99

100

101

102

103

104

105

106

107

108

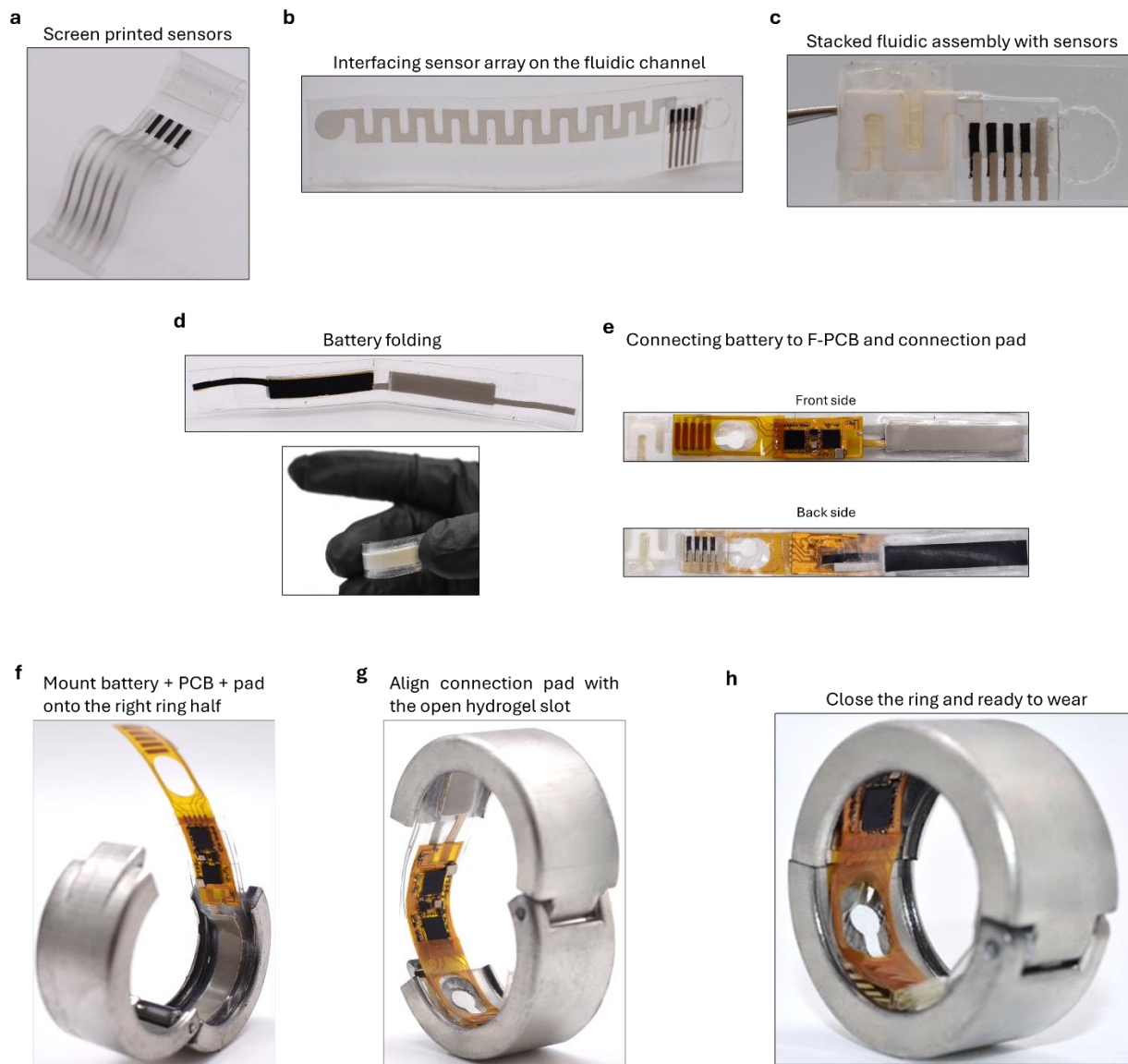
109

110

111

112

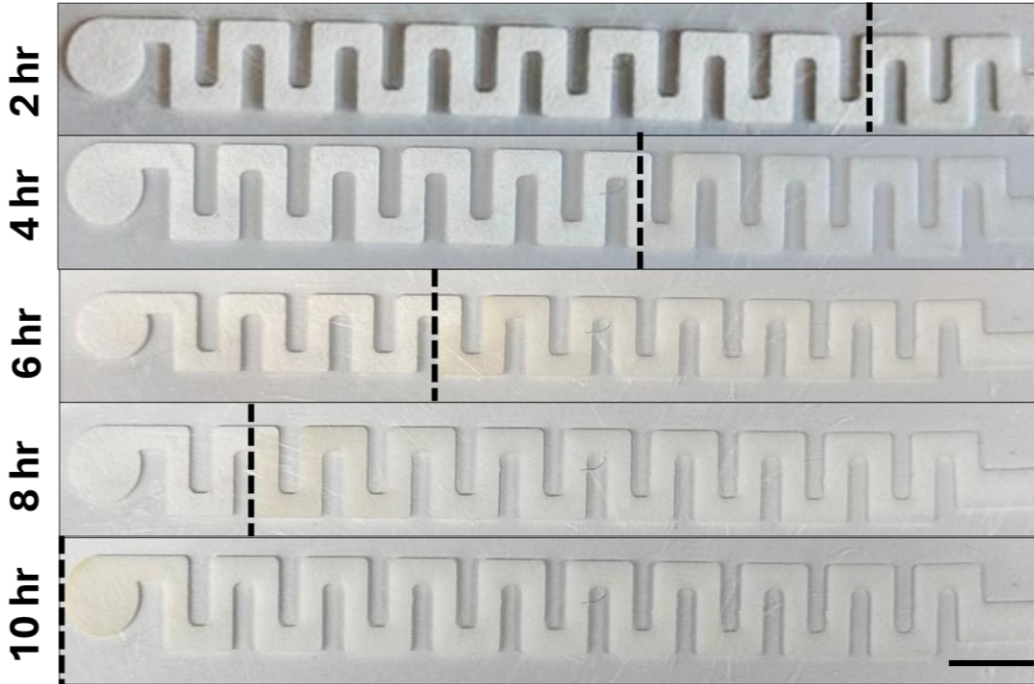
113



114

115 **Fig. S1:** CHARM assembling process. a) The electrode array are first screen printed on  
 116 SEBS and b) interfaced to the fluidic channel near the hydrogel inlet with SEBS casing.  
 117 c) The fluidic channel is then folded to reduce its length such that it fits in the ring. d) The  
 118 printed batteries are folded along the center and e) connected to the F-PCB on one end.  
 119 The other end of F-PCB connects to the electrical connections of the connection pad. The  
 120 pad has an elliptical slot to accommodate the hydrogel. Metallic array connections on the  
 121 other end of the connection pad connects to the printed electrochemical sensor array. f)  
 122 The whole assembly is fitted on the right half of CHARM and curved such that the  
 123 elliptical hole on the connector pad aligns with the hydrogel slot on the left half of  
 124 CHARM. The right half is pushed such that it locks, making CHARM ready for use.

125



126

127 **Fig. S2:** Optical image of the fluidic channel showing liquid advancement at 150 nl/min  
 128 flow rate. The fluid reaches the end of channel in about 10 hours. Scale bar: 5 mm.

129 **Supplementary Note 1: Theoretical estimation of hydrogel osmotic pressure**

130 The osmotic pressure of a hydrogel is derived theoretically by estimating the swelling  
 131 pressure using the Flory-Rehner Theory. The swelling capacity of any gel system upon  
 132 fluid intake is highly dependent on the overall contributions from elastic forces, polymer-  
 133 solvent interactions, and ionic composition. These effects depend on several  
 134 thermodynamic properties (e.g., temperature, pH, solution ionic strength and  
 135 composition). Hence, it is important to estimate each contribution to understand the  
 136 overall swelling behavior and fluid extraction capacity of a hydrogel.<sup>1-4</sup>

137 The total swelling pressure ( $\pi_{tot}$ ) is derived using the following equation:

138 
$$\pi_{tot} = -V_1^{-1} \left( \frac{\partial \Delta F_{tot}}{\partial n_1} \right) = \pi_{el} + \pi_{mix} + \pi_{ion} \quad (2)$$

139 where  $V_1$  is the solvent molar volume (18 ml/mol),  $n_1$  is the number of moles of solvent,  
 140  $\pi_{tot}$  is the total gel swelling pressure and  $\pi_{el}$ ,  $\pi_{mix}$  and  $\pi_{ion}$  are the elastic, mixing and  
 141 ionic contributions to the total swelling pressure, respectively.

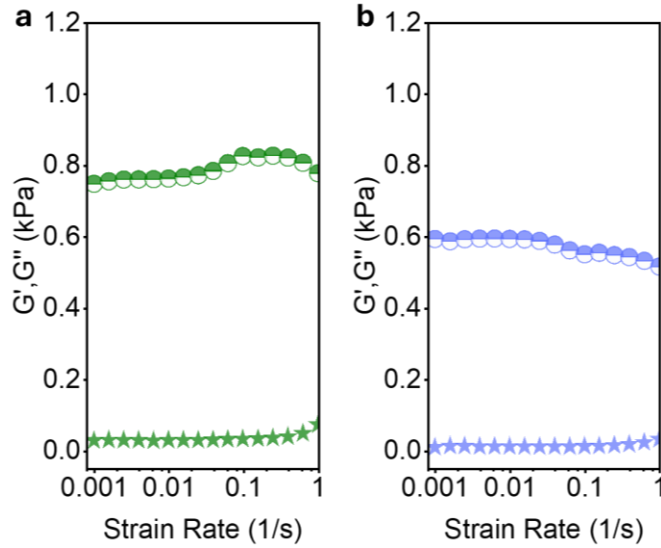
142 We first quantified the elastic contributions ( $\pi_{el}$ ) for all our hydrogel systems. For  
 143 every hydrogel variant, we estimated its weight swelling ratio ( $q_p$ ), polymer volume  
 144 fraction after equilibration ( $\phi_2$ ), and gel shear modulus ( $G$ ) via experiments. These  
 145 parameters were used for the estimation of  $\pi_{tot}$ . The  $q_p$  was calculated as:

146 
$$q_p = \frac{m_{gel}}{m_{dry}} \quad (3)$$

147 where  $m_{gel}$  is the initial mass of gel after equilibration in the osmolyte and  $m_{dry}$  is the  
 148 mass of gel after drying.  $\phi_2$  was calculated from  $q_p$  as follows:

149 
$$\phi_2 = \left[ 1 + \frac{(q_p - 1)\rho}{d} \right]^{-1} \quad (4)$$

150 where  $\rho$  is the polymer density (1.35 g/ml-PAAm, and 1.29 g/ml- PVA)<sup>5</sup> and  $d$  is the density  
 151 of water (1 g/ml).  $\phi_2$  (PVA – PAAm) = 0.18.



152  
 153 **Fig. S3:**  $G'/G''$  vs. strain rate plot of at angular frequency of 10 rad/s for a) PVA-PAAm gel  
 154 soaked in pure EG; and b) PVA-PAAm gel soaked in PBS. Circle:  $G'$ , Star:  $G''$ .

155 The elastic contribution in the hydrogel system using  $\phi_2$  was calculated as follows:

156 
$$\pi_{el} = -G = G_{dry}\phi_2^{1/3} \quad (5)$$

157 where  $G_{dry}$  is the dry gel shear modulus unequilibrated in any solution.  $G$  for both pure  
 158 EG and PBS hydrogel variants were measured through an amplitude sweep experiment  
 159 conducted at an angular frequency of 10 rad/s using a rheometer (TA instruments HR 30).  
 160  $G$  ranged  $\sim 0.8$  KPa and  $\sim 0.6$  KPa for PVA-PAAm/EG and PVA-PAAm/PBS, respectively  
 161 (**Fig. S3**)

162 The contribution from the polymer-solvent mixing interactions was calculated as follows:

163 
$$\pi_{mix} = \frac{-RT}{V_1} [\ln(1 - \phi_2) + \phi_2 + \chi\phi_2^2] \quad (6)$$

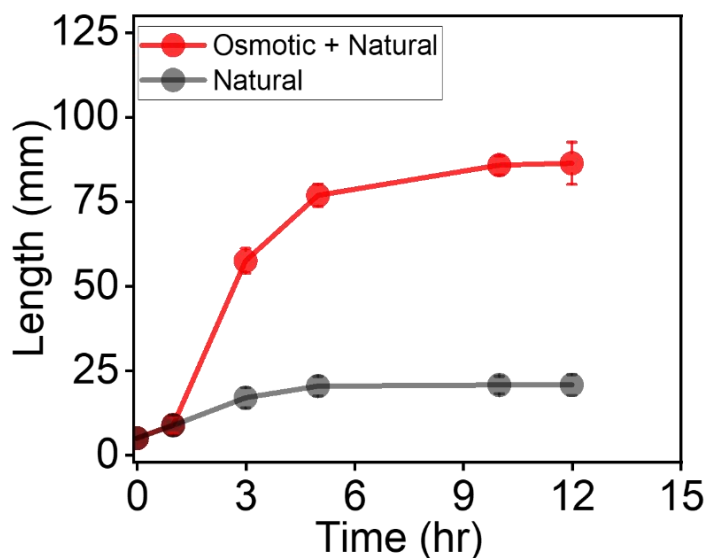
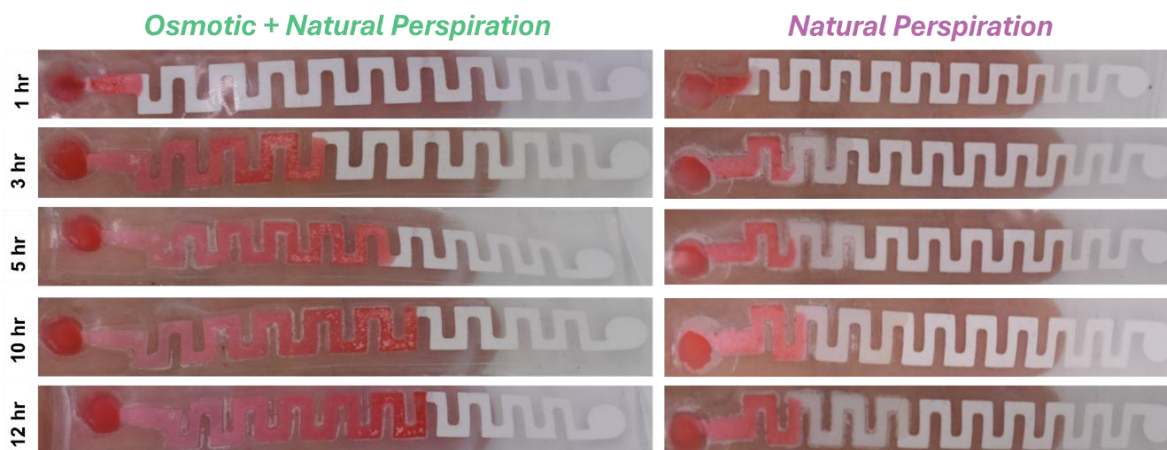
164 where  $\chi$  is the Flory-Huggins polymer-solvent interaction parameter. For hydrogels,  $\chi =$   
 165 0.48.<sup>6</sup>

166 The contributions from the ionic interactions were neglected as the hydrogels were not  
167 treated with any ionic solvent during the test.

168 The contributions from the ionic interactions are calculated as follows:

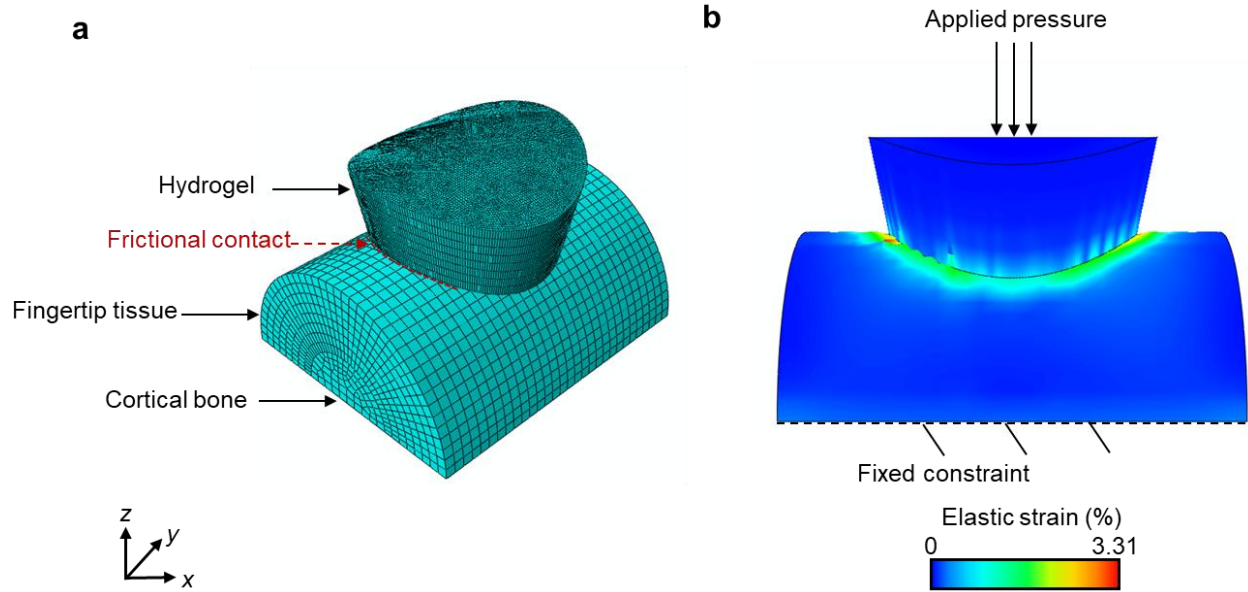
$$169 \quad \pi_{ion} = 2RT\{[(C^{sol})^2 + (i\phi_2/(2V_m))^2]^{0.5} - C^{sol}\} \quad (7)$$

170 where  $R$  is the gas constant,  $T$  is the absolute temperature,  $i$  is the degree of ionization,  
171  $V_m$  is the molar volume of the monomer unit of the polymer (13.50 mol/m<sup>3</sup>) and  $C^{sol}$  is the  
172 concentration of the electrolyte with which the gel is treated.<sup>3</sup> For DI, we assumed  $\pi_{ion}=0$ .  
173 For 1X PBS, we assumed  $C^{sol} = 0.1 \frac{mol}{L}$  and  $i = 2$  (since NaCl is the dominant salt).  
174 Based on this,  $\pi_{tot} = 2.79 MPa$  and  $58 kPa$  were estimated for PVA PAAm (pure EG) and  
175 PVA PAAm (PBS), respectively.



176  
177 **Fig. S4:** Optical image of the fluidic channel showing greater dye penetration due to  
178 osmosis vs. natural perspiration. Experiments were conducted at the ring finger site.

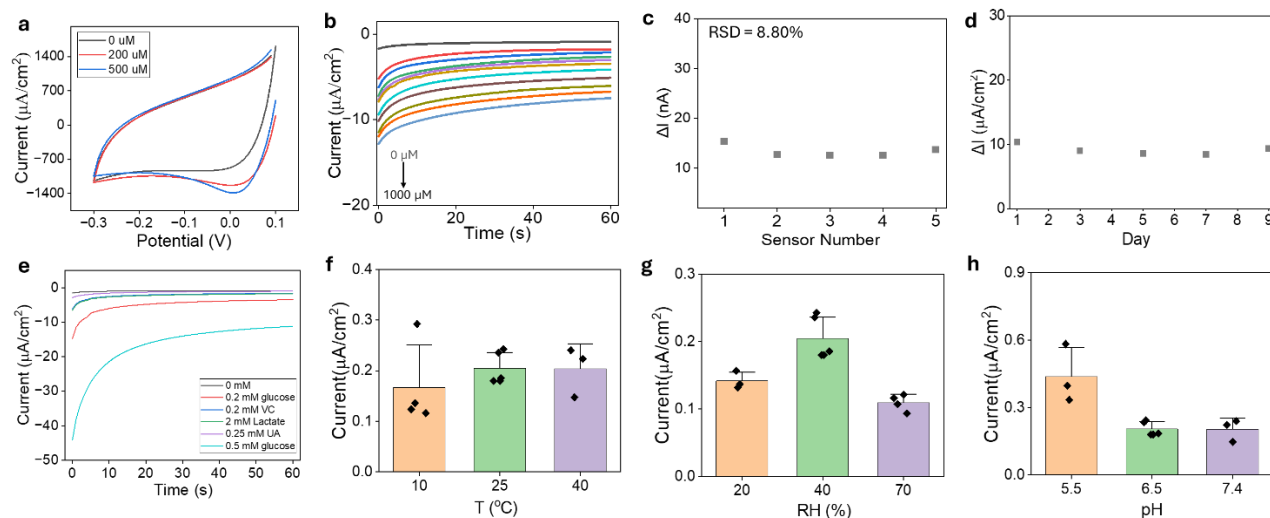
179 **Supplementary Note 2: Von Mises stress estimation on hydrogel surface**



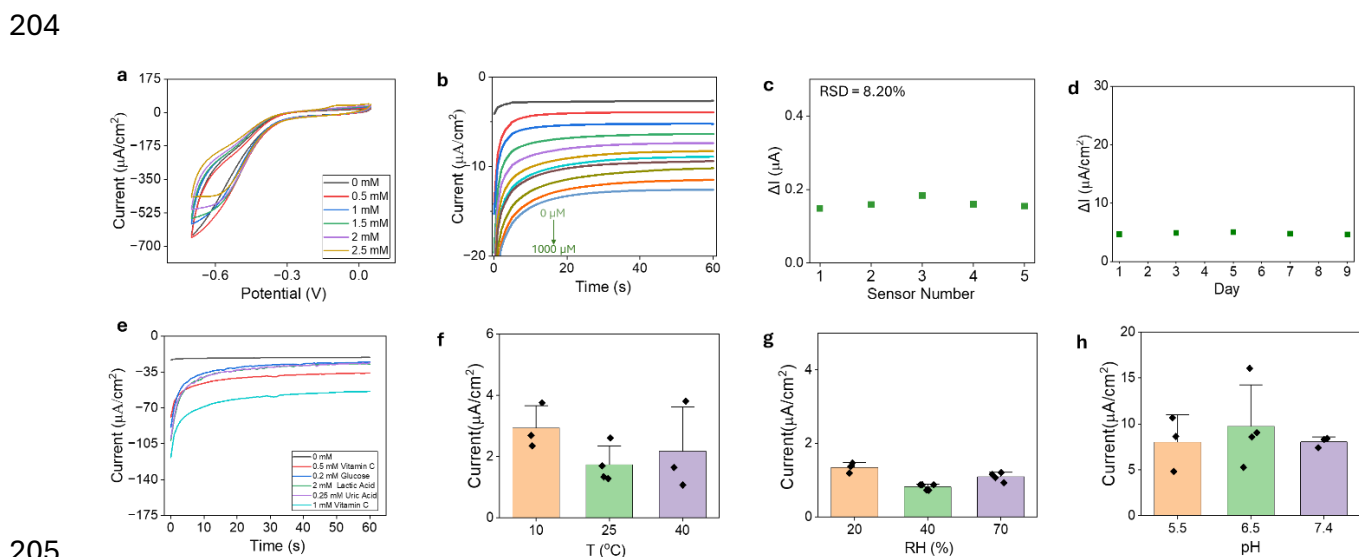
181 **Fig. S5:** Mechanical simulation of the hydrogel under bending. a, Isometric view of the  
182 assembled meshed system with defined frictional contact between the hydrogel and  
183 fingertip tissue. b, Lateral view of the elastic strain on fingertip tissue after applying 3 KPa  
184 pressure on the hydrogel surface.

185 The commercial software ABAQUS was utilized to predict the stresses acting on the  
186 hydrogel and fingertip interface under an applied pressure. An 8-node linear brick,  
187 reduced integration (C3D8R) mesh (**Fig. S5**) and explicit dynamic analysis were adopted  
188 to ensure the convergence of the simulations. Frictional contact between the hydrogel  
189 interface and fingertip tissue was defined with a frictional coefficient of  $\mu = 0.15$ .<sup>7</sup>  
190 Hyperelastic properties were defined by fitting the experimental stress-strain data of the  
191 hydrogel. Here, we chose Neo-Hookean hyperelastic model to calculate the coefficients  
192 of the hydrogel  $C_{10} = 785.25$  and  $D_1 = 0.00137$ . Linear elastic properties were used to  
193 model the fingertip skin and cortical bone where the elastic modulus  $E$  and Poisson's ratio  
194  $\nu$  are  $E_{\text{Skin}} = 400$  KPa and  $\nu_{\text{Skin}} = 0.48$ ;  $E_{\text{Cortical bone}} = 16.2$  GPa and  $\nu_{\text{Cortical bone}} = 0.36$ .<sup>8,9</sup>  
195 We assumed that human skin could accommodate up to  $\sim 30\%$  elastic strain and used  
196 this as a conservative upper-bound stretchability when estimating the strain in the skin  
197 layer induced by applying 3 kPa normal pressure to the hydrogel surface.

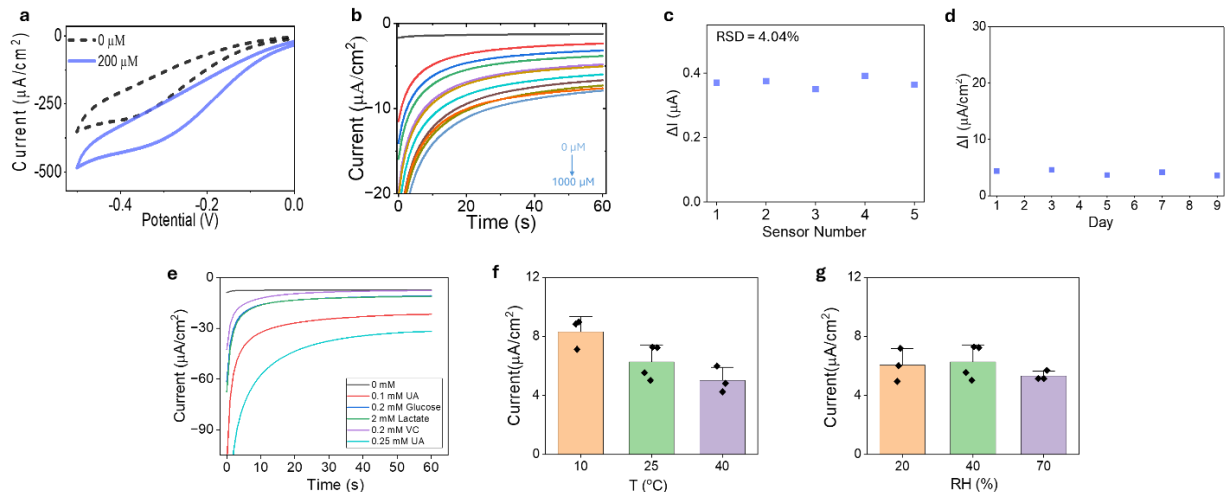
198



199  
 200 **Fig. S6:** In-vitro performance of the glucose sensor showing a) cyclic voltammetry (CV);  
 201 b) chronoamperometric response with 100  $\mu\text{M}$  increments; c) Relative standard deviation  
 202 (RSD) from 5 sensors; d) Long-term stability of the sensor response; e) interference plot;  
 203 stability under varying f) temperature, g) relative humidity (RH), and h) pH.

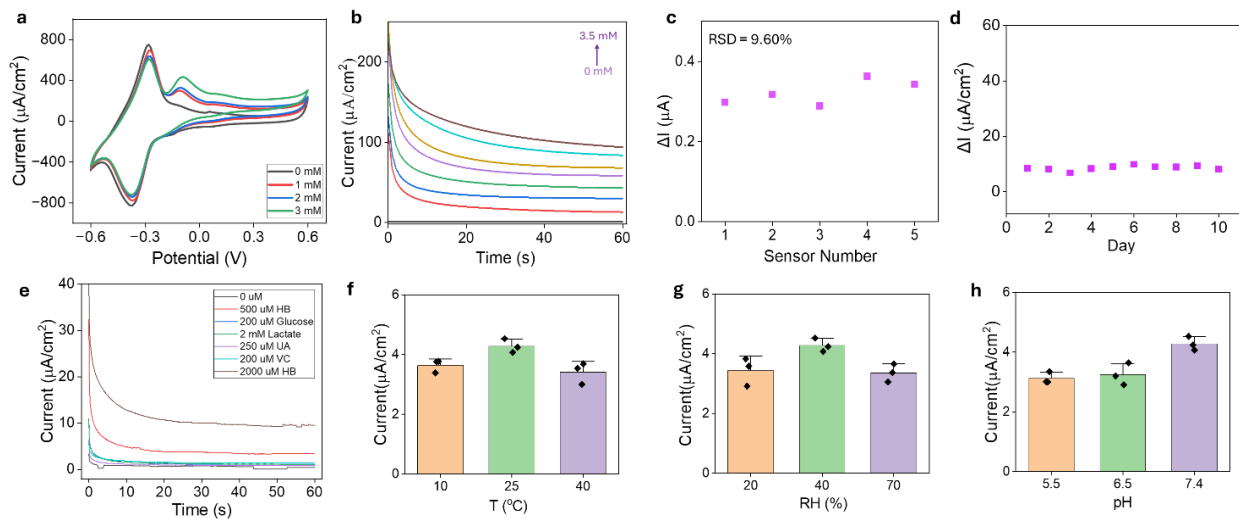


205  
 206 **Fig. S7:** In-vitro performance of the ascorbic acid sensor showing a) cyclic voltammetry  
 207 (CV); b) chronoamperometric response with 100  $\mu\text{M}$  increments; c) Relative standard  
 208 deviation (RSD) from 5 sensors; d) Long-term stability of the sensor response; e)  
 209 interference plot; stability under varying f) temperature, g) relative humidity (RH), and h)  
 210 pH. The response follows an inverse trend with pH at a rate of  $\sim -0.20 \frac{\mu\text{A}\cdot\text{cm}^{-2}}{\text{pH}}$ .



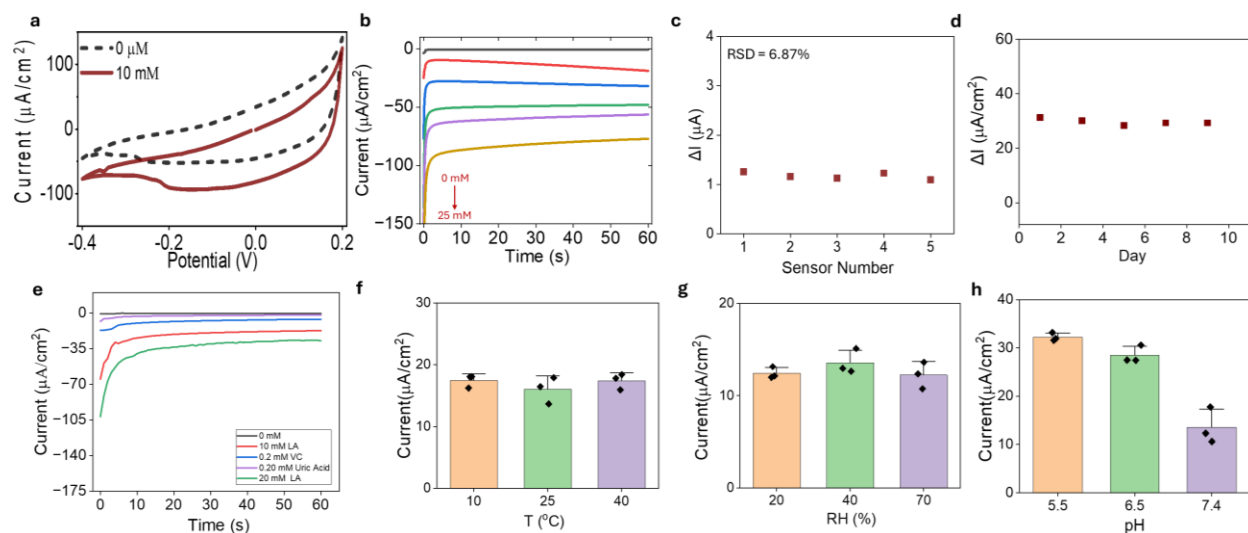
212

213 **Fig. S8:** In-vitro performance of the uric acid sensor showing a) cyclic voltammetry (CV);  
 214 b) chronoamperometric response with 100  $\mu\text{M}$  increments; c) Relative standard deviation  
 215 (RSD) from 5 sensors; d) Long-term stability of the sensor response; e) interference plot;  
 216 stability under varying f) temperature, and g) relative humidity (RH).

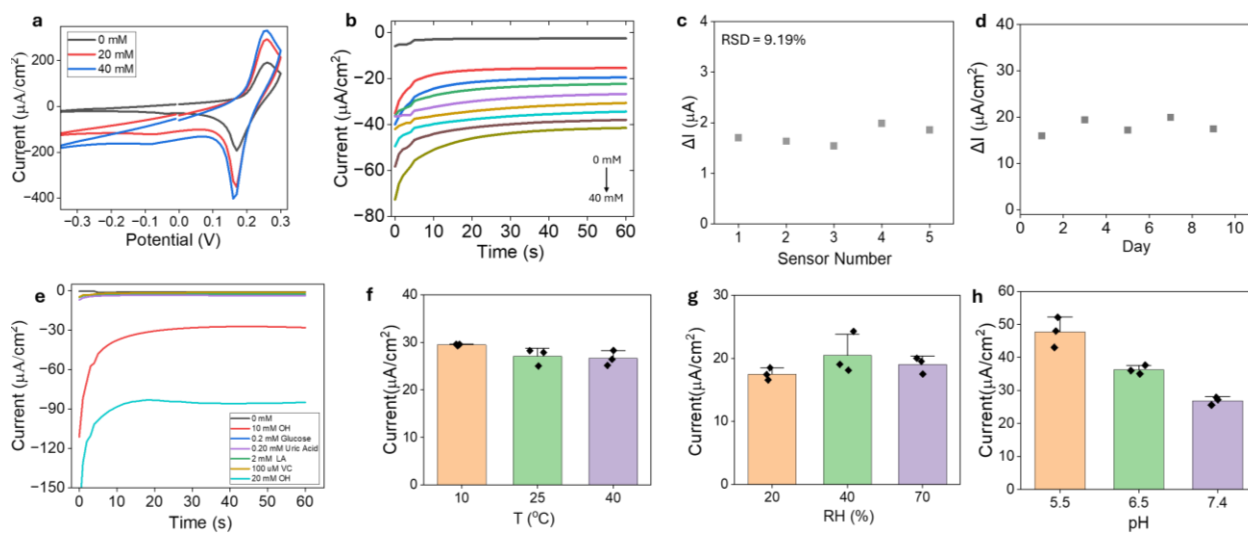


217

218 **Fig. S9:** In-vitro performance of the ketone sensor showing a) cyclic voltammetry (CV);  
 219 b) chronoamperometric response with 0.5 mM increments; c) Relative standard deviation  
 220 (RSD) from 5 sensors; d) Long-term stability of the sensor response; e) interference plot;  
 221 stability under varying f) temperature, g) relative humidity (RH), and h) pH. The response  
 222 follows an inverse trend with pH at a rate of  $\sim 5.40 \frac{\mu\text{A}\cdot\text{cm}^{-2}}{\text{pH}}$ .



223  
 224 **Fig. S10:** In-vitro performance of the lactate sensor showing a) cyclic voltammety (CV);  
 225 b) chronoamperometric response with 5 mM increments; c) Relative standard deviation  
 226 (RSD) from 5 sensors; d) Long-term stability of the sensor response; e) interference plot;  
 227 stability under varying f) temperature, g) relative humidity (RH), and h) pH. The response  
 228 follows an inverse trend with pH at a rate of  $\sim -9.10 \frac{\mu A.cm^{-2}}{pH}$ .



229  
 230 **Fig. S11:** In-vitro performance of the alcohol sensor showing a) cyclic voltammety (CV);  
 231 b) chronoamperometric response with 5mM increments; c) Relative standard deviation  
 232 (RSD) from 5 sensors; d) Long-term stability of the sensor response; e) interference plot;  
 233 stability under varying f) temperature, g) relative humidity (RH), and h) pH. The response  
 234 follows an inverse trend with pH at a rate of  $\sim -0.77 \frac{\mu A.cm^{-2}}{pH}$ .

236 **Supplementary Note 3: Numerical simulation of analyte flux under varying**  
 237 **concentrations and sweat rates**

238 Finite element simulations were performed using COMSOL Multiphysics to model the  
 239 experimental system in a simplified two-dimensional framework. A fully wetted paper  
 240 channel operating under incompressible conditions was assumed, and mass  
 241 conservation was enforced through the continuity equation (Eq. S1). Consistent with the  
 242 low-Reynolds number regime characteristic of paper-based microfluidic systems ( $Re <$   
 243  $1$ ), the flow was treated as laminar, in agreement with previous reports on lateral flow  
 244 assays.<sup>10</sup> Under these assumptions, fluid transport within the channel was modeled using  
 245 the Brinkman-modified Navier–Stokes equations to capture the effects of porosity,  
 246 permeability, and viscous drag in the porous matrix confined between two parallel plates  
 247 (Eq. S1).<sup>11</sup>

248 The channel geometry, along with the initial and boundary conditions applied in the  
 249 simulations, are shown in Figure S1. Transport of the electroactive analyte was modeled  
 250 using the convection–diffusion equation (Fick’s second law, Eq. S2). The rate constant  
 251  $K$  was experimentally determined from chronoamperometric measurements conducted at  
 252 varying analyte concentrations. A linear relationship between the steady-state current  $I$   
 253 and concentration  $C$  was observed (**Fig. 2d**), validating the first-order reaction  
 254 assumption. To capture the sensor response under a fixed applied overpotential (i.e.,  
 255 chronoamperometric operation), the Butler–Volmer kinetics were simplified to a first-order  
 256 reaction with respect to analyte concentration,  $J_i = -K_i C_i$ , representing the time-  
 257 dependent consumption of analyte at the electrode surface.<sup>12</sup> The subscript  $i$  represents  
 258 the different tested analytes: glucose, BHB, lactate, UA, UC, and ethanol.

259

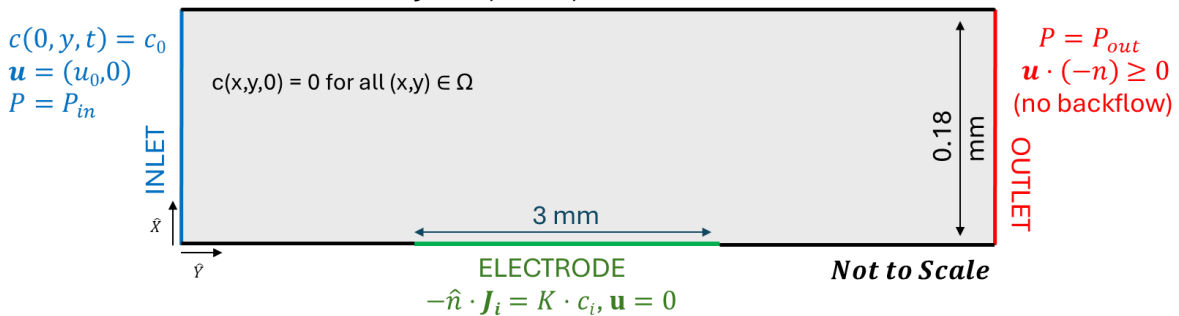
$$(Eq. S1) \quad \frac{\rho}{\epsilon} \frac{\partial \mathbf{u}}{\partial t} = -\nabla P + \mu_{eff} \nabla^2 \mathbf{u} - \frac{k}{\mu} \mathbf{u}, \quad \nabla \cdot \mathbf{u} = 0$$

$$(Eq. S2) \quad \frac{\partial c_i}{\partial t} + \mathbf{u} \cdot \nabla c_i = D_{i,eff} \nabla^2 c_i, \quad \text{where } \mathbf{J}_i = -D_{i,eff} \nabla c_i + \mathbf{u} c_i$$

$$\mathbf{u} = (u_{i,x}, u_{i,y}), \quad \mathbf{J}_i = (J_{i,x}, J_{i,y})$$

$$\mathbf{u} = (0,0) \quad (\text{no slip \& penetration}),$$

$$\text{WALL} \quad -\hat{n} \cdot \mathbf{J} = 0 \quad (\text{no flux})$$



260

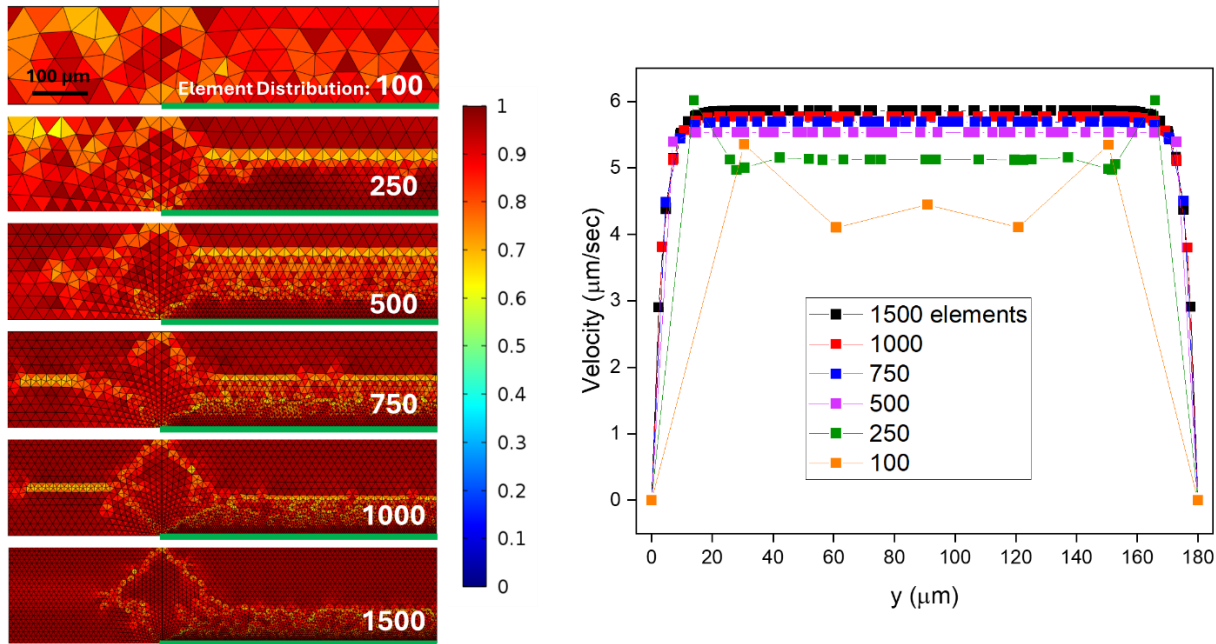
261 **Fig. S12:** Schematic illustration and mathematical formulation of the fluid flow numerical  
 262 model. Equation S1 describes fluid flow using the Navier–Stokes equations with Brinkman  
 263 corrections, while Equation S2 governs analyte transport via the convection–diffusion  
 264 equation. The parameters  $\rho$ ,  $\mu$ ,  $\epsilon$ ,  $\kappa$ ,  $\tau$ , and  $D$  represent the solution density and dynamic  
 265 viscosity, paper porosity, permeability, tortuosity, and the diffusion coefficient of the  
 266 analyte, respectively. The effective viscosity and diffusion coefficient are defined as  $\mu_{\text{eff}} =$   
 267  $\mu/\epsilon$  and  $D_{\text{eff}} = \epsilon D/\tau$ . The variables  $u$ ,  $J$ ,  $p$ ,  $c$ , and  $t$  denote the velocity and flux fields,  
 268 pressure, analyte concentration, and time, respectively; bold symbols indicate vector  
 269 quantities, and subscripts  $x$  and  $y$  denote their corresponding components. The subscript  
 270  $i$  represents the different tested analytes: glucose, BHB, lactate, UA, UC, and ethanol.  
 271 The parameter  $K$  corresponds to the experimentally determined sensor sensitivity. All  
 272 parameter values used in the simulations are listed in **Table S1**.

273 **Table S1.** Parameters, symbols, and values used in the numerical simulation.

Name	Symbol	Value	Units
Paper porosity (fraction of void volume)	$\epsilon$	0.7	-
Faraday Constat	$F$	96485.3	sA mol <sup>-1</sup>
Temperature	$T$	293.15	K
Water Dynamic viscosity	$\mu$	0.89	mPa s
Water density	$\rho$	997.0	Kg m <sup>-3</sup>
Paper permeability	$\kappa$	10e-12	m <sup>2</sup>
Glucose diffusion coefficient	$D_{\text{Glu}}$	7.1e-10	m <sup>2</sup> s <sup>-1</sup>
BHB diffusion coefficient	$D_{\text{BHB}}$	6.6e-10	m <sup>2</sup> s <sup>-1</sup>
Lactate diffusion coefficient	$D_{\text{Lac}}$	1.1e-9	m <sup>2</sup> s <sup>-1</sup>
UA diffusion coefficient	$D_{\text{UA}}$	6.7e-10	m <sup>2</sup> s <sup>-1</sup>
VC diffusion coefficient	$D_{\text{VC}}$	6.4e-10	m <sup>2</sup> s <sup>-1</sup>
Ethanol diffusion coefficient	$D_{\text{Eth}}$	1.2e-9	m <sup>2</sup> s <sup>-1</sup>
Glucose reaction rate constat	$K_{\text{Glu}}$	4.5e-7	m <sup>3</sup> A mol <sup>-1</sup>
BHB reaction rate constat	$K_{\text{BHB}}$	1.7e-6	m <sup>3</sup> A mol <sup>-1</sup>
Lactate reaction rate constat	$K_{\text{Lac}}$	1.2e-7	m <sup>3</sup> A mol <sup>-1</sup>
UA reaction rate constat	$K_{\text{UA}}$	1.4e-6	m <sup>3</sup> A mol <sup>-1</sup>
VC reaction rate constat	$K_{\text{VC}}$	7.3e-7	m <sup>3</sup> A mol <sup>-1</sup>
Ethanol reaction rate constat	$K_{\text{Eth}}$	2.9e-8	m <sup>3</sup> A mol <sup>-1</sup>

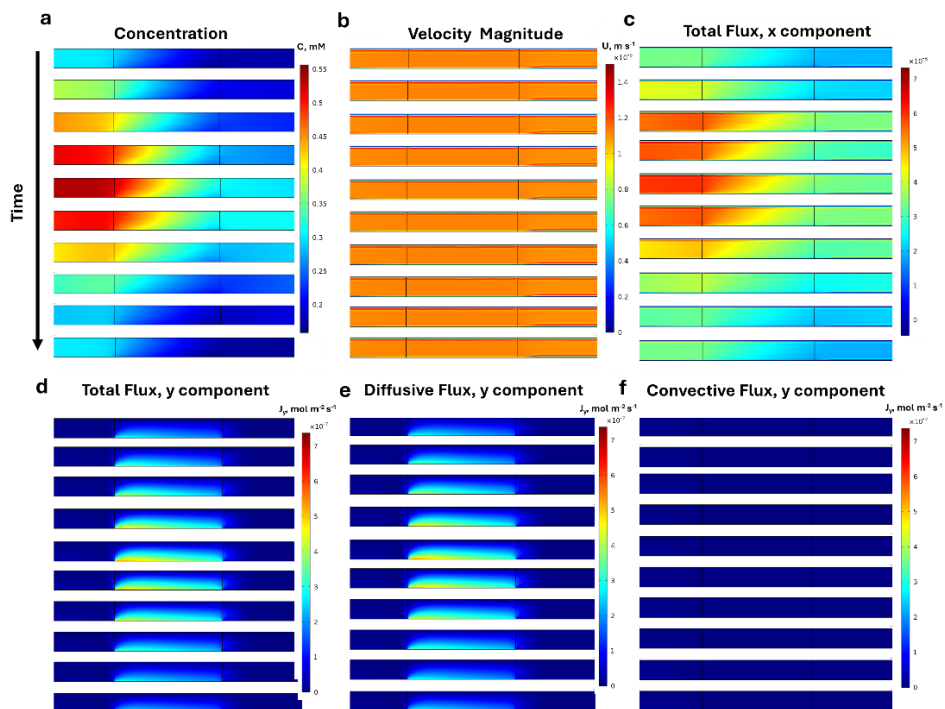
274

275



276

277 **Fig. S13:** Mesh Convergence and Numerical Validation. Mesh convergence was verified  
 278 by progressively refining the mesh and evaluating the channel velocity profile across the  
 279 channel. Mesh level 5 was selected, with 1,000 elements distributed along the sensor  
 280 line, as further refinement produced less than a 1% change in velocity. The final mesh  
 281 consisted of approximately 60,000 elements and required a solving time of under 10  
 282 minutes. The resulting velocity profile exhibited plug-like flow, consistent with porous  
 283 paper channels.



284

285 **Fig. S14:** Transient numerical simulation showing time-dependent inlet concentration  
286 changes. The inlet analyte concentration was ramped from 0.30 to 0.55 mM and then  
287 ramped down to 0.30 mM, each over 200 s, with a 600 s hold period between ramps. The  
288 flow velocity was kept constant throughout the entire simulation. The following parameters  
289 were monitored and plotted: (a) analyte concentration, showing the increase and  
290 decrease in spatial concentration distribution in response to changes at the inlet; (b)  
291 absolute velocity, which remained constant as expected; (c) total analyte flux in the x  
292 direction, increasing with inlet concentration primarily due to convection along the  
293 channel; (d) total analyte flux in the y direction, exhibiting significant flux along the sensor  
294 line and negligible flux elsewhere; (e) diffusive component of the analyte flux in the y  
295 direction, matching the magnitude and spatial distribution of the total y-direction flux; and  
296 (f) convective component of the analyte flux in the y direction, showing no contribution,  
297 as expected. Time stamps: 0,10,13,16,19,22,25,28,31,40 mins.

#### 298 **Supplementary Note 4. Electronic system overview and control architecture**

299 The wearable sensing system consists of a low-power Bluetooth-enabled microcontroller  
300 unit (MCU; nRF52840) and an analog front-end (AFE; AD5940). The firmware implements  
301 a deterministic finite-state control architecture that minimizes average power  
302 consumption while maintaining reproducible electrochemical measurements.

303 The control program operates cyclically and comprises three primary modes: (i)  
304 chronoamperometric data acquisition, (ii) buffered wireless data transmission, and (iii) a  
305 low-power sleep interval. During each cycle, electrochemical data are acquired and  
306 stored locally in memory, transmitted wirelessly in a short burst after acquisition is  
307 complete, and followed by a prolonged low-power idle period before the next acquisition  
308 cycle begins.

##### 309 1.1 Chronoamperometric acquisition protocol

310 Chronoamperometric (CA) measurements are performed sequentially across four  
311 electrodes using a software-controlled switch matrix. For each electrode configuration,  
312 data rate, excitation voltage, and sampling period are all individually adjustable.

313 The four electrode configurations are measured consecutively in a user-defined order.  
314 The AFE generates measurement-ready events that are detected by the MCU, and the  
315 MCU reads and stores the corresponding current values. The AFE remains active only  
316 during the acquisition phase and is explicitly shut down after completing the fourth  
317 channel to reduce static power consumption.

##### 318 1.2 Firmware state machine and timing control

319 The firmware is implemented as an explicit state machine with four main states:  
320 initialization, acquisition, transmission, and sleep. After system initialization, the firmware

321 enters the acquisition state, during which chronoamperometric measurements are  
322 performed sequentially across the four electrode configurations. A sample counter tracks  
323 the number of measurements acquired per channel and triggers a state transition once  
324 the predefined number of samples is reached.

325 Upon completion of data acquisition, the firmware transitions to the transmission state,  
326 during which the BLE radio is enabled, and the locally buffered data is transmitted to an  
327 external receiver in bursts. After successfully transmitting all stored samples, the firmware  
328 enters a low-power sleep state for a predefined interval before restarting the cycle.

### 329 1.3 Data buffering and wireless transmission

330 All electrochemical data are stored locally in the MCU's memory during the acquisition  
331 phase. Data is organized sequentially by channel and time and is not transmitted in real  
332 time. This buffering strategy enables the BLE radio to remain disabled during sensing,  
333 thereby reducing radio duty cycle and minimizing interference between wireless  
334 communication and electrochemical measurements.

335 During the transmission state, buffered data are packetized and transmitted via BLE  
336 notifications. Each packet includes metadata indicating the electrode configuration and  
337 sample index to ensure correct reconstruction of the time series at the receiver. After all  
338 buffered data is transmitted, the BLE stack is explicitly de-initialized to prevent  
339 background radio activity during subsequent low-power operation.

### 340 1.4 Low-power operation and duty cycling strategy

341 To minimize average power consumption, the firmware employs aggressive duty cycling  
342 of high-power subsystems. The BLE radio and associated high-frequency clocks are  
343 enabled only during the short transmission window following data acquisition. During the  
344 acquisition phase, BLE is disabled, and only the AFE and required MCU peripherals are  
345 active.

346 After data transmission, the AFE is placed into a shutdown state, and all wireless  
347 communication interfaces are disabled. The MCU then enters a low-power idle state  
348 implemented using a delay-based sleep mechanism, which was empirically found to yield  
349 the lowest baseline current consumption on this platform. The sleep interval was set to 6  
350 min, substantially longer than the acquisition and transmission durations, ensuring that  
351 the system spent most of its operating cycle in a low-power state while continuously  
352 acquiring meaningful CA data.

### 353 1.5 Watchdog-based autonomous restart

354 Rather than preserving MCU state across sleep intervals, the system employs a  
355 watchdog-timer-based restart mechanism. A hardware watchdog timer is configured to

356 reset the MCU after the sleep interval elapses. Upon reset, the firmware restarts from a  
357 known initial state and initiates a new acquisition cycle.

358 This approach eliminates the need to retain RAM or peripheral state during sleep,  
359 reducing idle-state power consumption, and ensures robust long-term operation without  
360 cumulative state drift. Using a full system reset also simplifies the firmware design and  
361 improves fault tolerance.

#### 362 **Supplementary Note 5. Debug and deployment configurations**

363 Two firmware configurations are used during development and testing. In a debug  
364 configuration, USB serial communication is enabled to allow real-time logging and  
365 diagnostic output. In a deployment (low-power) configuration, all USB-related functionality  
366 is disabled to reduce baseline current consumption. The functional behavior of the control  
367 program is otherwise identical between configurations. The circuit is programmed using  
368 a custom-designed desktop probe station. Firmware flashing is done using an NRF52840  
369 development kit with the NRF Connect desktop software.

#### 370 **Supplementary Note 6. Power consumption measurement methodology 1**

371 Power consumption measurements are performed with the system powered via the  
372 custom-designed desktop probe station and a Nordic Power Profiler Kit. Current  
373 consumption is displayed and recorded in real time using the power profiler tool GUI on  
374 a PC, and characteristic current levels are recorded for the acquisition, transmission, and  
375 sleep phases.

376 Distinct current plateaus corresponding to the acquisition phase, the BLE transmission  
377 burst, and the low-power sleep interval are observed, confirming the correct operation of  
378 the duty-cycled control program. Disabling USB and BLE during sleep results in a  
379 substantial reduction in baseline current compared to debug configurations.

#### 380 **Supplementary Note 7. Power consumption measurement methodology 2**

381 The received signal strength indicator (RSSI) of the BLE communication is characterized  
382 using a smartphone-based application (nRF Toolbox, Nordic Semiconductor). During  
383 these measurements, the circuit operates in its standard transmission mode, in which  
384 buffered data are transmitted via BLE notifications after the acquisition phase completes.

385 RSSI measurements are performed in a laboratory environment with a maximum  
386 separation distance of 3 m between the circuit and the smartphone. The smartphone  
387 receiver is held stationary at each measurement location to minimize motion-induced  
388 variability. RSSI values are recorded over multiple transmission cycles to evaluate the  
389 stability and consistency of the wireless link under typical operating conditions. These  
390 measurements are intended to provide a practical assessment of communication range  
391 and link quality rather than a calibrated radio-frequency characterization.

392 **Supplementary Note 8. Power consumption measurement methodology 3**

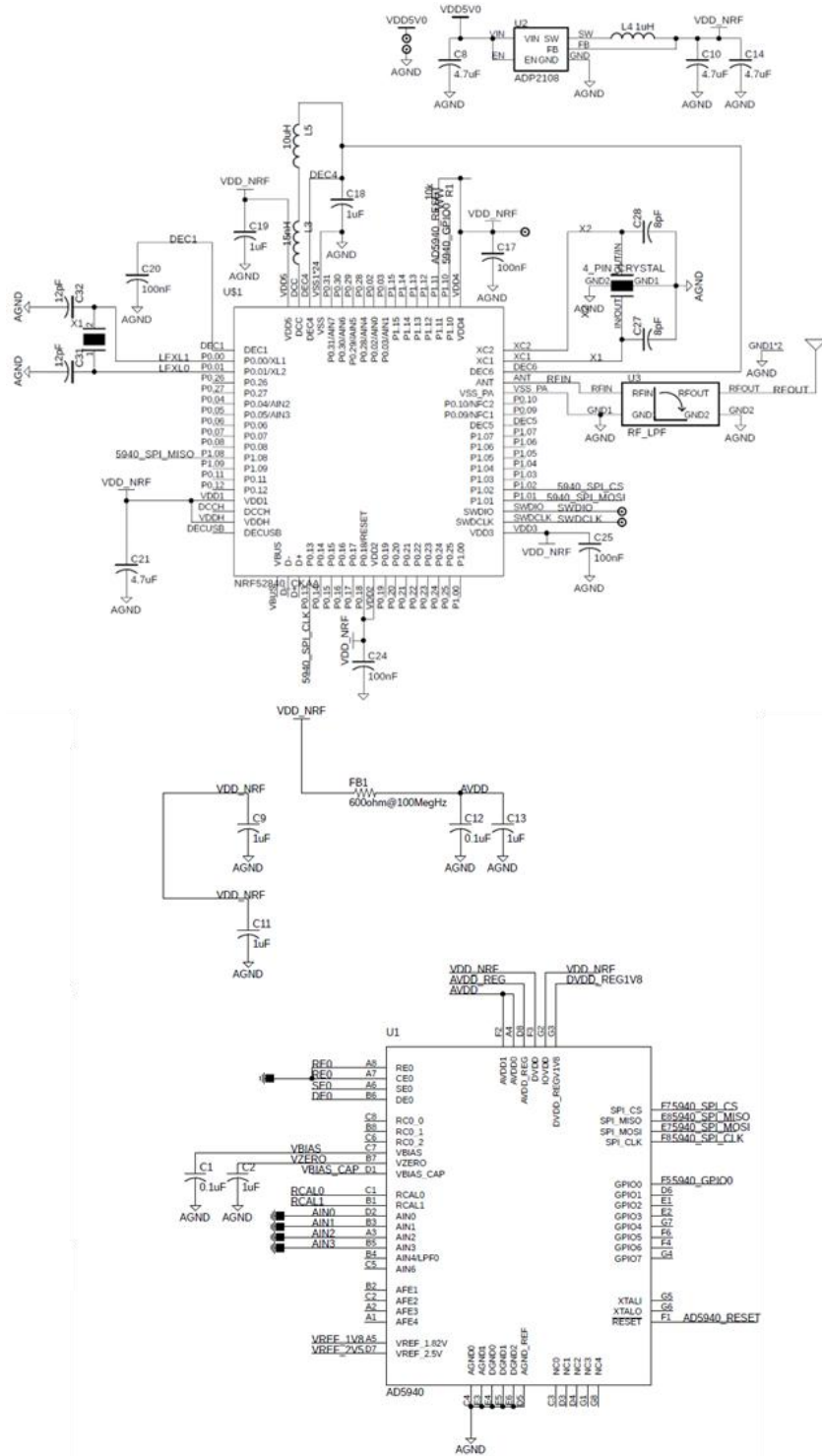
393 Thermal imaging is performed to assess temperature changes of the wearable circuit  
394 during a complete operating cycle. Thermal images are acquired with an infrared thermal  
395 camera (FLIR C5) at 0 s, 60 s, 300 s, and 600 s after the start of a measurement cycle.  
396 These points span the full sequence of electrochemical acquisition, wireless data  
397 transmission, and low-power sleep.

398 Over the 10 min operating cycle, the device's maximum surface temperature increases  
399 from 27.3 °C at the start to 31.0 °C at the end. The observed temperature rise is gradual  
400 and stabilizes during the latter portion of the cycle, consistent with the system's duty-  
401 cycled operation, in which high-power activities are confined to short acquisition and  
402 transmission intervals.

403 The measured temperature increase remains well within ranges considered safe for  
404 prolonged skin-contact wearable electronics, indicating that the device does not produce  
405 excessive thermal loading during normal operation.

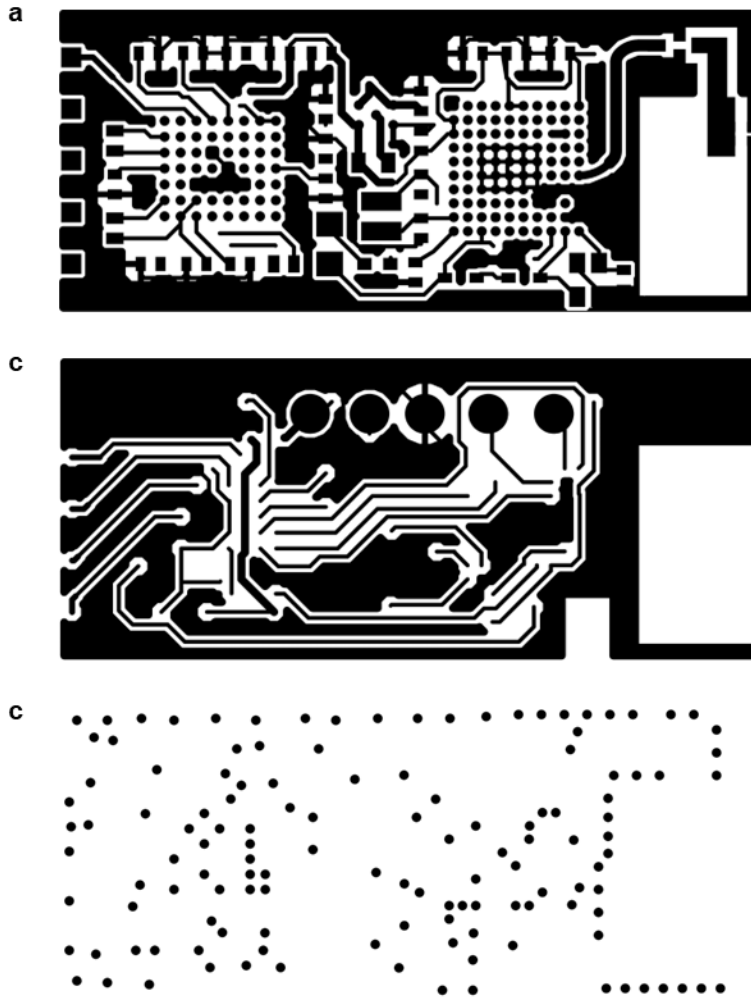
406

407



408

409 **Fig. S15:** Circuit schematics. The circuit comprises three major components: the  
 410 microcontroller unit (MCU, NRF52840, Nordic Semiconductor), the analog front end  
 411 (AFE, AD5940, Analog Devices), and a power converter (ADP2108, Analog Devices). All  
 412 components are selected to minimize board area while maintaining high sensitivity, low  
 413 noise, and low power consumption.



414

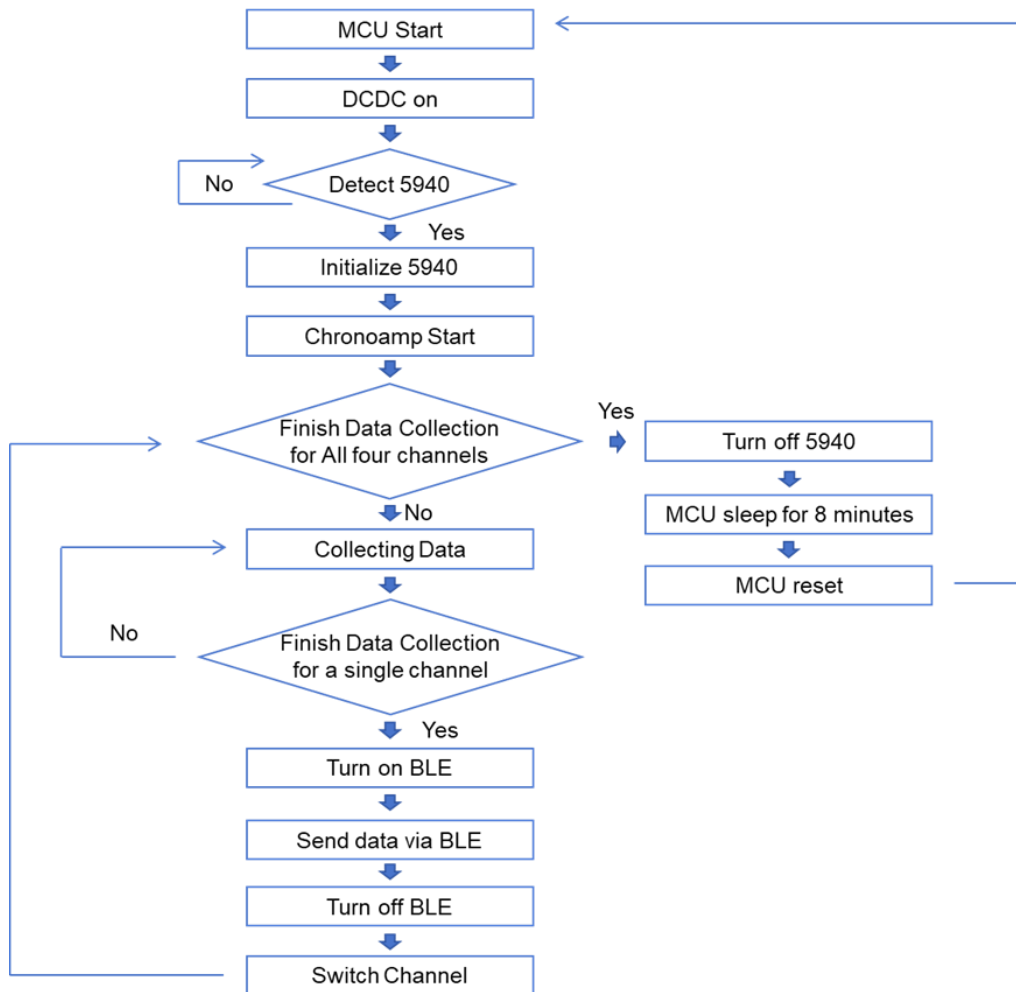
415 **Fig. S16:** F-PCB layer and drill layout. a. fPCB top layer copper pattern, large areas of  
 416 copper fill are applied to simplify routing in a compact area while maintaining good noise  
 417 suppression and RF transmittivity; b. fPCB bottom layer copper pattern. Thin copper  
 418 traces (75  $\mu\text{m}$ ) are used to fan out the delicate BGA chips properly; c. fPCB drill vertical  
 419 interconnect access (VIA) drill pattern. Stitched VIAs are applied along the board edge  
 420 and in the RF antenna region to minimize ingress noise and radiated emissions back into  
 421 the board.

422

Qty	Value	Footprint Name	Parts
4	0.47uF	C0201	C3, C4, C6, C7
6	100nF	C0201	C1, C12, C17, C20, C24, C25
1	10uH	IND_0402	L5
2	12pF	C0201	C31, C32
1	15nH	IND_0201	L3
6	1uF	C0201	C2, C9, C11, C13, C18, C19
1	1uH	IND_0302	L4
1	LF Crystal	LF Crystal	X1
5	4.7uF	C0201	C5, C8, C10, C14, C21
1	HF Crystal	HF Crystal	X2
1	600ohm@100MegHz	R0201	FB1
2	8pF	C0201	C27, C28
1	AD5940	AD5940	U1
1	ADP2108	ADP2108	U2
1	ANT_2450AT07A0100	2450AT07A0100	ANT1
1	NRF52840_CKAA	NRF52840	U\$1
1	RF_LPF	2450LP07C0100	U3

423

424 **Fig. S17:** Bill of materials. The table shows the component values, footprint, and parts  
 425 name used to assemble the circuit. 0201 package is used whenever possible to save the  
 426 board size.

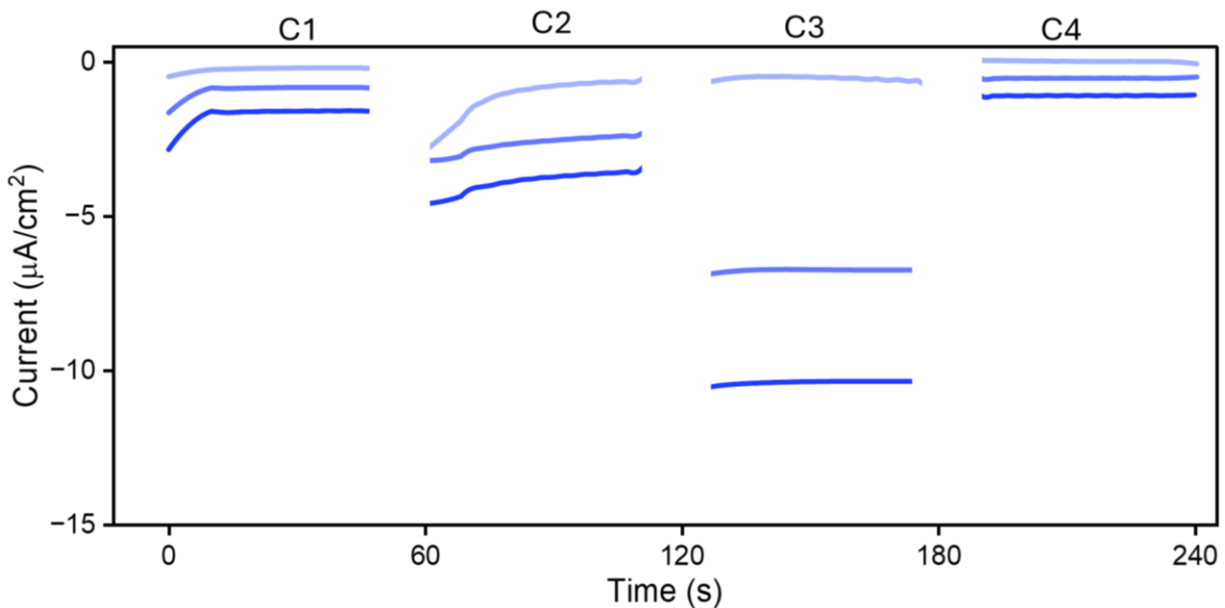


427

428 **Fig. S18:** Low-power control flow chart. The low-power sensing program starts by  
 429 enabling the MCU's DC-DC converter to reduce MCU power consumption. It then detects

430 whether the AFE is appropriately connected. If yes, the AFE is initialized, and the  
431 chronoamperometry at the first sensor location starts. Then, Bluetooth Low Energy (BLE)  
432 is enabled to wirelessly transmit the data to a receiver, after which it is shut down again  
433 for power savings. The AFE then switches to the next channel and repeats this three more  
434 times before entering the idle state. It then sleeps for 8 minutes before starting a new  
435 round of sensing.

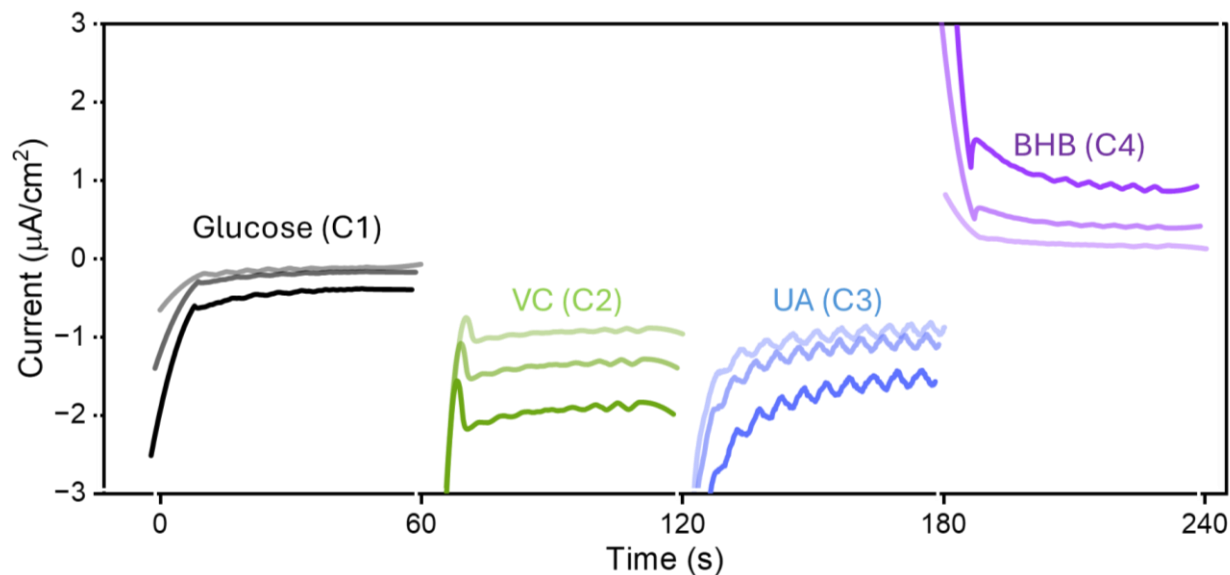
436



437

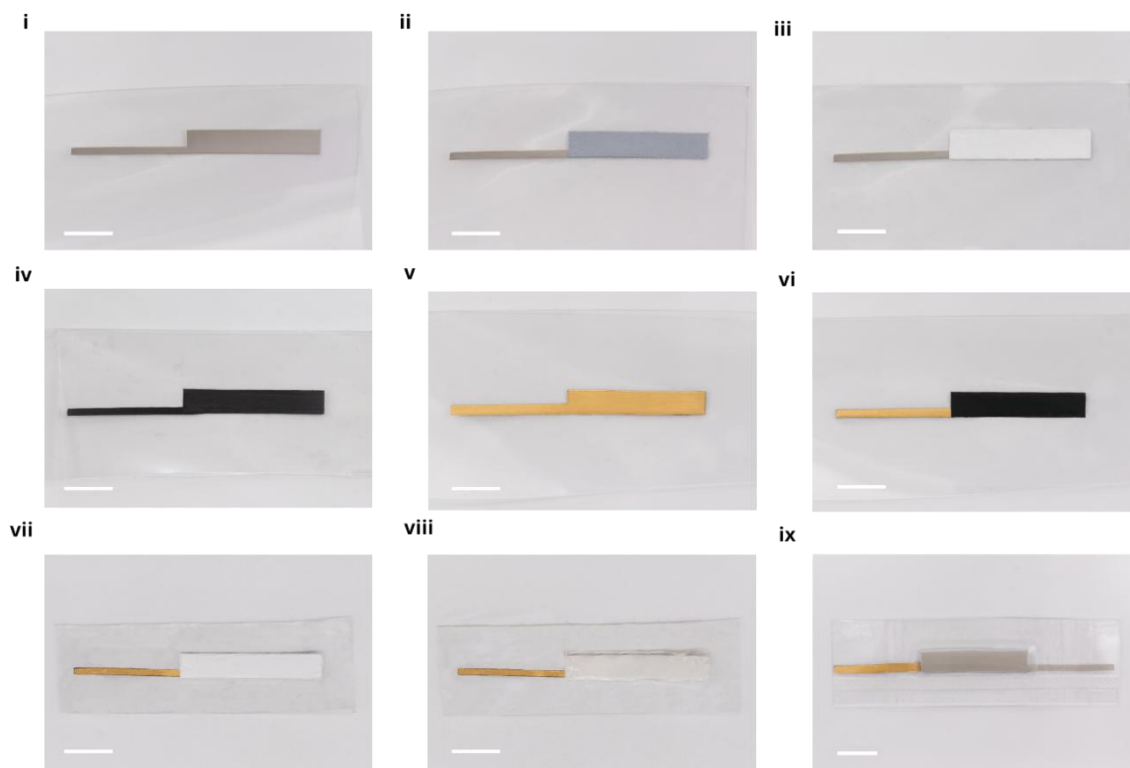
438 **Fig. S19:** Chronoamperometric response from 4 channels in the F-PCB, operating  
439 sequentially for peroxide detection in a Prussian blue-carbon electrode system. C1:  
440 Channel 1 at -0.05V, C2: Channel 2 at -0.5V, C3: Channel 3 at -0.3V, and C4: Channel 4  
441 at 0.05V. All four working electrodes shared a common reference electrode. Peroxide  
442 concentrations spiked: 0,500,1000 µM.

443



444

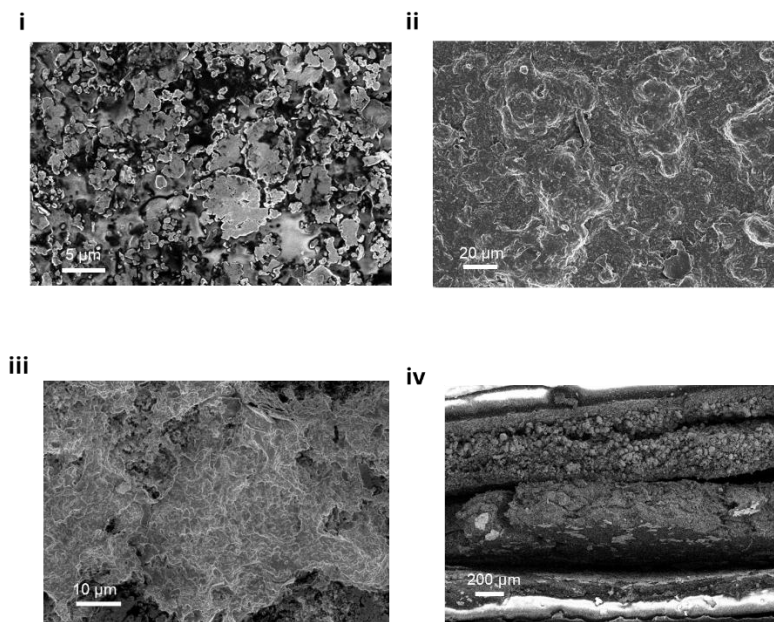
445 **Fig. S20:** Chronoamperometric response from 4 channels in the F-PCB, operating  
 446 sequentially for glucose, VC, UA, and BHB detection at their respective potentials.  
 447 Glucose concentrations: 0,200,500  $\mu\text{M}$ ; VC concentrations: 0,200,400  $\mu\text{M}$ ; UA  
 448 concentrations: 0,100,400  $\mu\text{M}$ ; BHB concentrations: 0,400,1000  $\mu\text{M}$ . All four working  
 449 electrodes shared a common reference electrode.



450

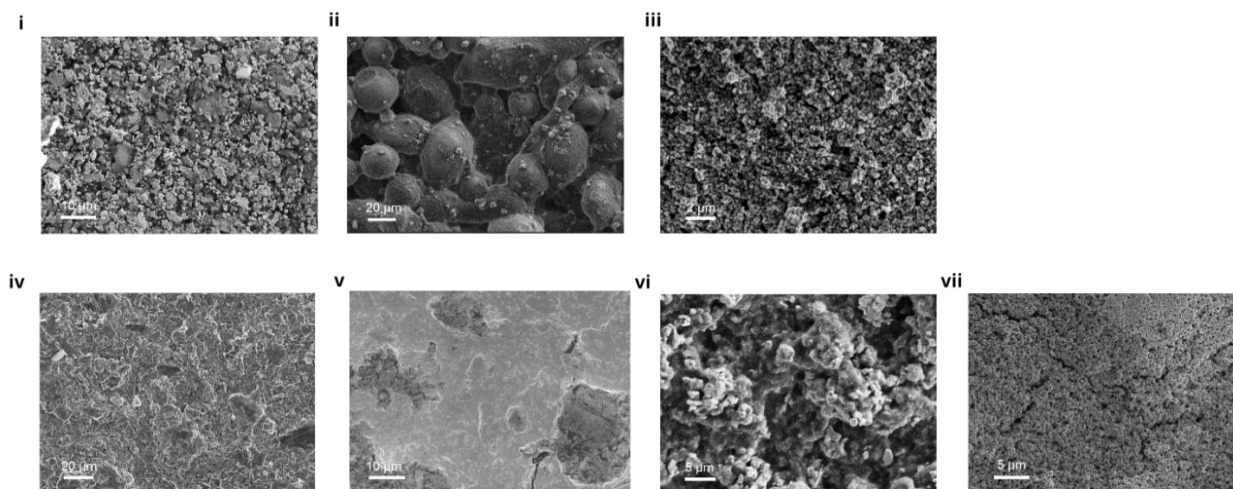
451 **Fig. S21.** Optical images of the layer-by-layer printing of the flexible AgO-Zn battery. (i)  
 452 Ag current collector; (ii) Zn anode; (iii)  $\text{TiO}_2$  separator; (iv) carbon current collector; (v)

453 Sputtered Au; (vi) AgO cathode; (vii) cellulose separator; (viii) hydrogel electrolyte; (ix)  
454 assembled battery. Scale bar: 1 cm.



455  
456 **Fig. S22.** SEM images of the Ag CC (i), carbon CC (ii), gold sputtered CC (iii) layers and  
457 full cell (iv) of the flexible AgO-Zn battery.

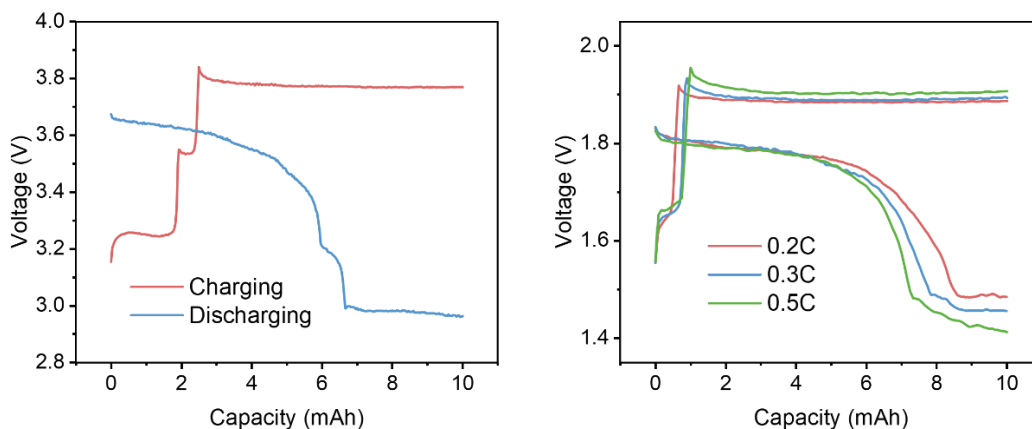
458



459  
460 **Fig. S23.** SEM images of the different layers of the flexible AgO-Zn battery after bending.  
461 (i) AgCC; (ii) zinc anode; (iii) TiO<sub>2</sub> separator; (iv) carbon CC; (v) gold sputter; (vi) AgO;  
462 (vii) cellulose separator.

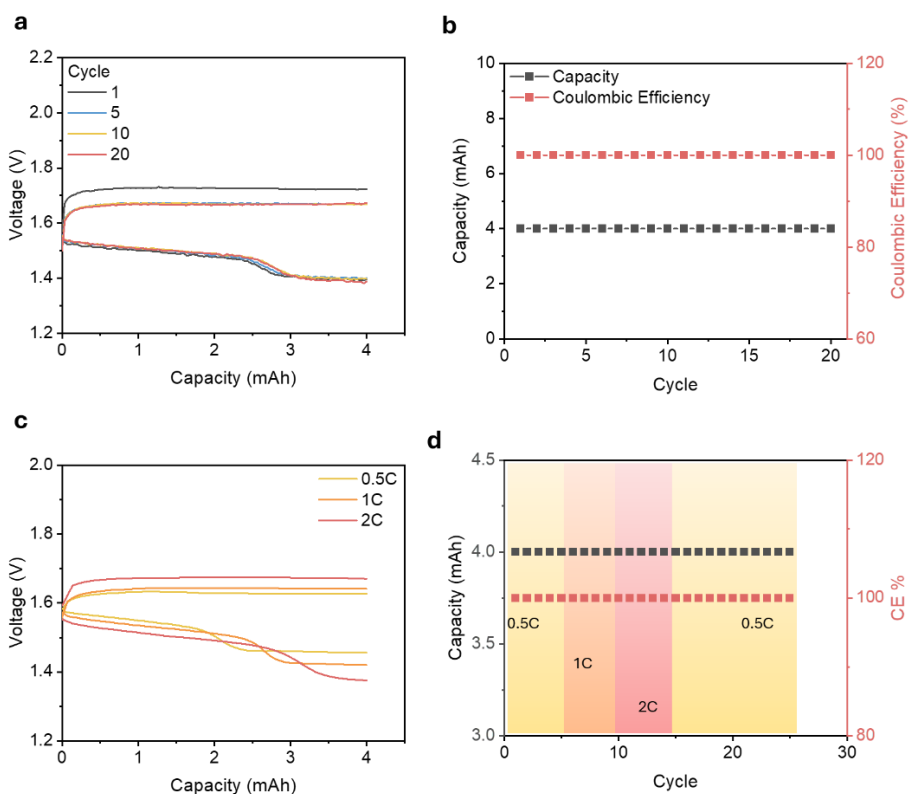
463

464



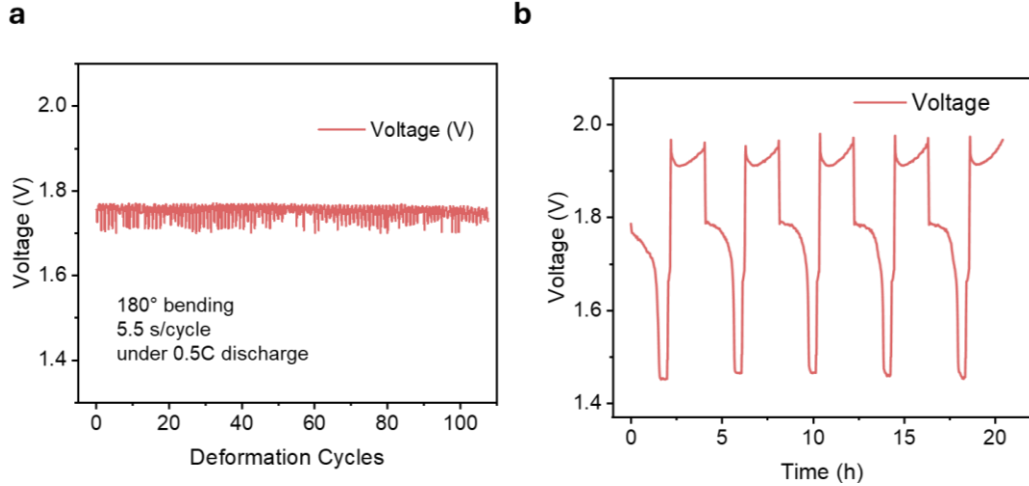
465  
 466 **Fig. S24.** (a) The voltage-capacity plot of the in series connected batteries. (b) The  
 467 voltage-capacity plot of the battery charging and discharging under different C-rates.

468



469  
 470 **Fig. S25.** (a) The voltage-capacity plot of the battery under 0.5 C-rate. (b) The cycling  
 471 performance of the battery at charging and discharging rates of 0.5 C. (c) The voltage-  
 472 capacity plot of the AgO-Zn flexible battery under different discharging C-rate. (d) The  
 473 cycling performance of the battery at different charging and discharging C-rates.

474



475

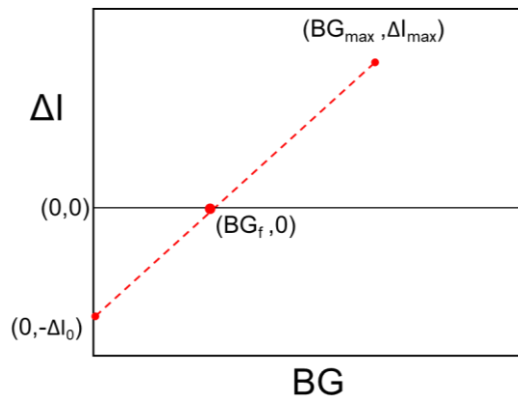
476 **Fig. S26.** (a) The voltage of AgO-Zn battery under 0.5C discharging intensity as well as  
 477 under 180° bending. (b) The voltage-time plot of battery for 5 repeat charging and  
 478 discharging cycles under 90° bending.

479

480 **Supplementary Note 9: Calibration model to acquire blood concentration dynamics**  
 481 **from sensor's  $I(t)$**

482 The two-point calibration model is developed by plotting minimum and maximum values  
 483 of  $\Delta I(t)$  vs  $BG(t)$ . The basis of this assumption is:

- 484 1. When  $\Delta I(t) = 0$ ,  $BG(t) = BG_f$
- 485 2.  $SBG(t) \rightarrow BG(t)$  will give minimum mean absolute relative difference (MARD).



486

487 From the calibration curve, the corrected slope ( $m$ ) is given by:

488 
$$m = \frac{\Delta I_{max}}{BG_{max} - BG_f}$$

489

490 and  $SBG(t) = \frac{I(t) - I_i + \Delta I_0}{m}$

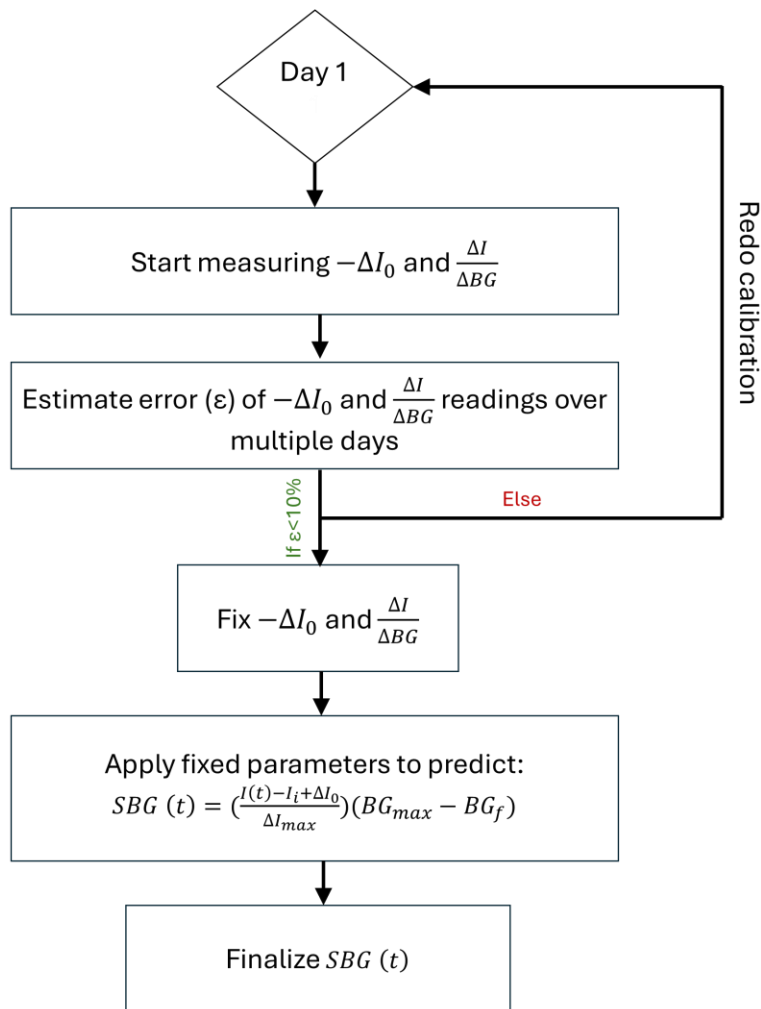
491 After substituting all values, the final derived equation to convert  $E(t)$  is:

492

$$SBG(t) = \left( \frac{I(t) - I_i + \Delta I_0}{\Delta I_{max}} \right) (BG_{max} - BG_f)$$

493

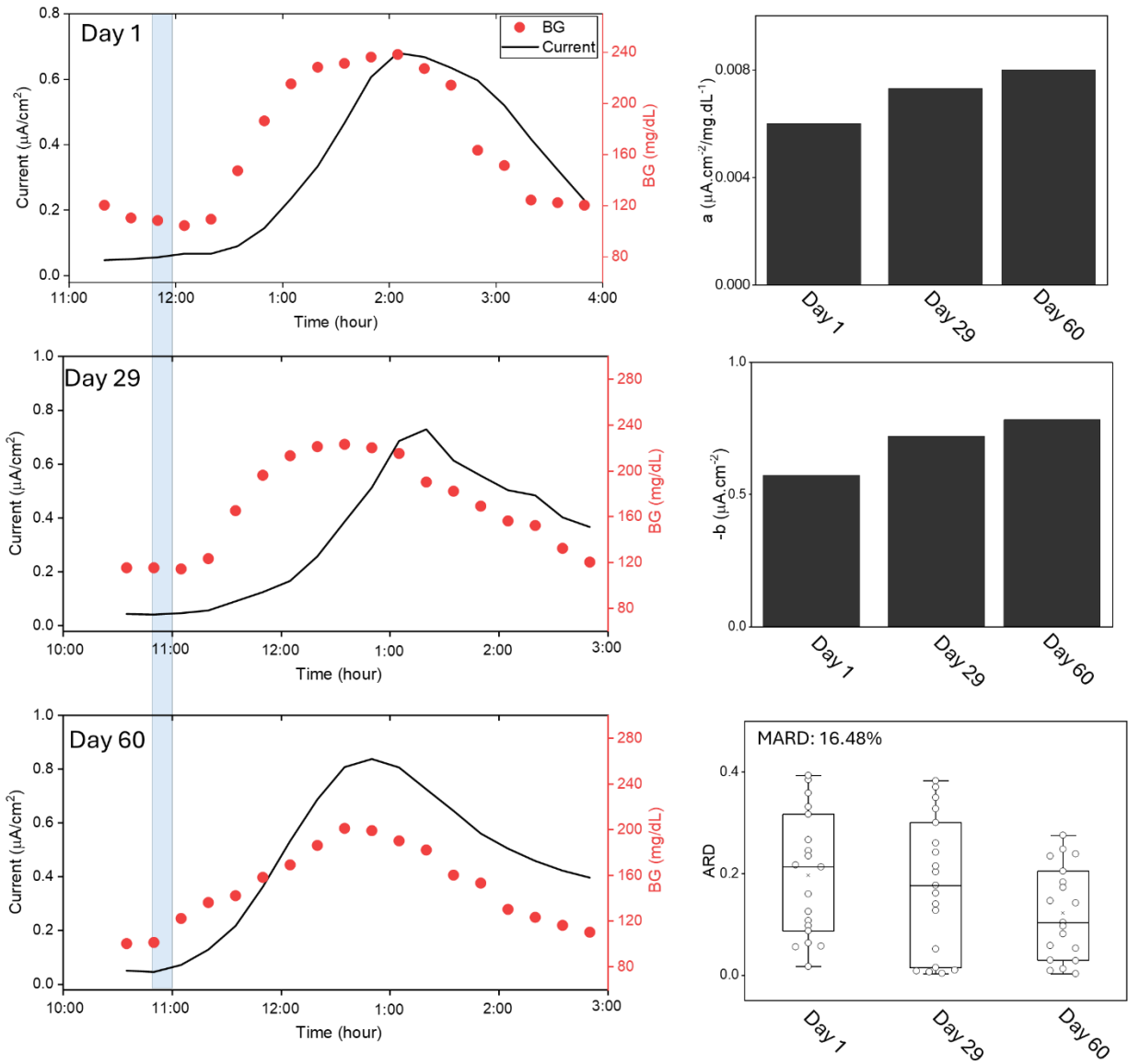
494



495

496 **Fig. S27:** Flow chart of personalized calibration protocol for glucose. The long-term  
497 stability of  $-\Delta I_0$  and  $\frac{\Delta I}{\Delta BG}$  under same stimulus determines the accuracy of  $SBG(t)$   
498 measurements.

499



500

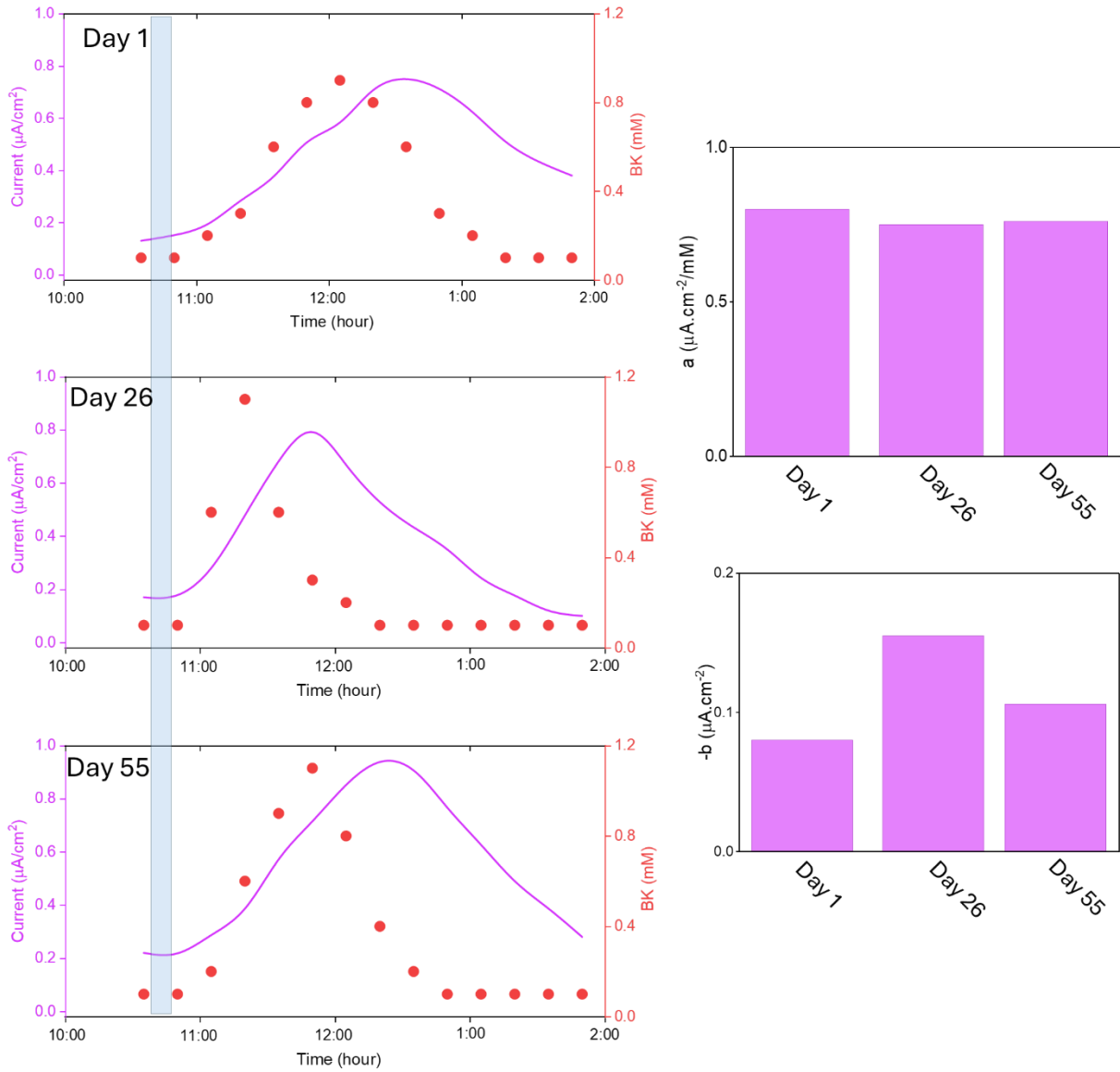
501 **Fig. S28:** Glucose profile of T1D subject over multiple days. Personalized coefficients  $a$   
 502 and  $b$  were evaluated on each day and their average ranged  $0.007 \frac{\mu A \cdot cm^{-2}}{mg \cdot dL^{-1}}$  and  
 503  $-0.65 \mu A \cdot cm^{-2}$ , respectively. Using these values, the average MARD from three tests  
 504 ranged  $\sim 16.48\%$ . Blue zone: Meal intake timeline.

505

506

507

508



509

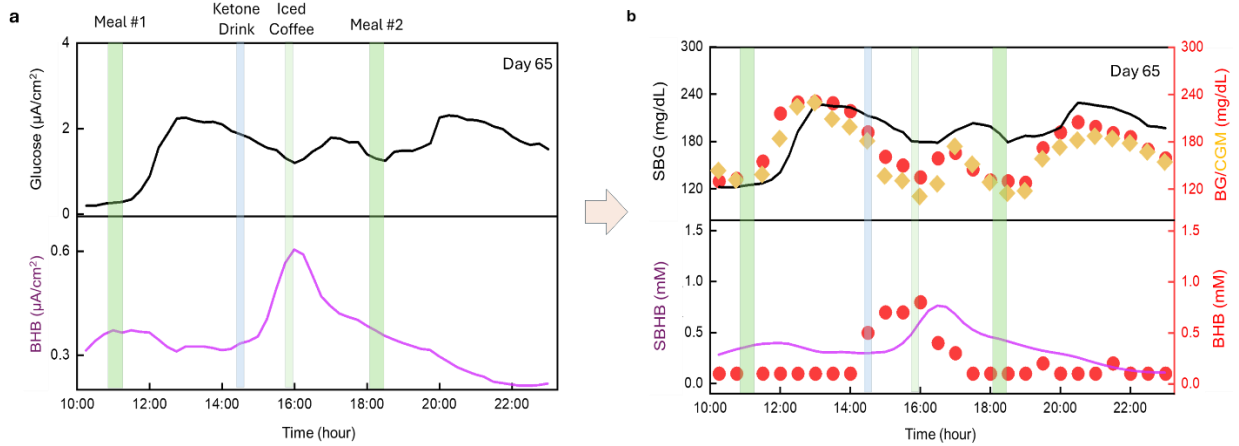
510 **Fig. S29:** Ketone profile of T1D subject over multiple days. Personalized coefficients  $a$   
 511 and  $b$  were evaluated on each day and their average ranged  $0.074 \frac{\mu\text{A}\cdot\text{cm}^{-2}}{\text{mg}\cdot\text{dL}^{-1}}$  and  
 512  $-0.113 \mu\text{A}\cdot\text{cm}^{-2}$ , respectively. Blue zone: Ketone drink intake timeline.

513

514

515

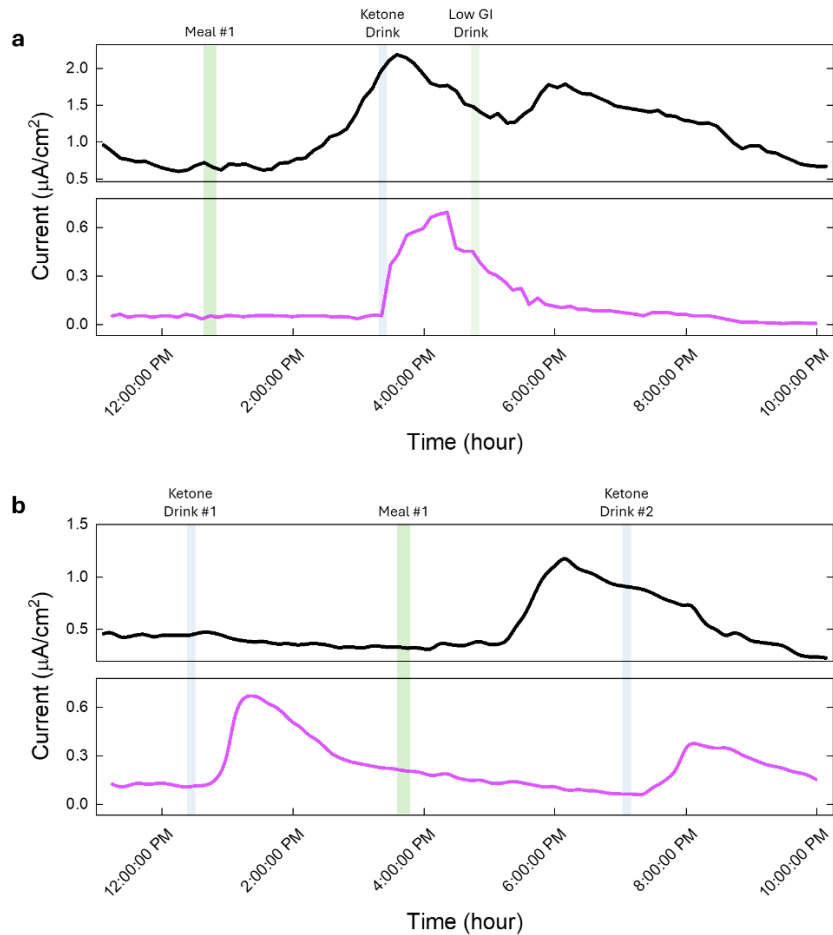
516



517

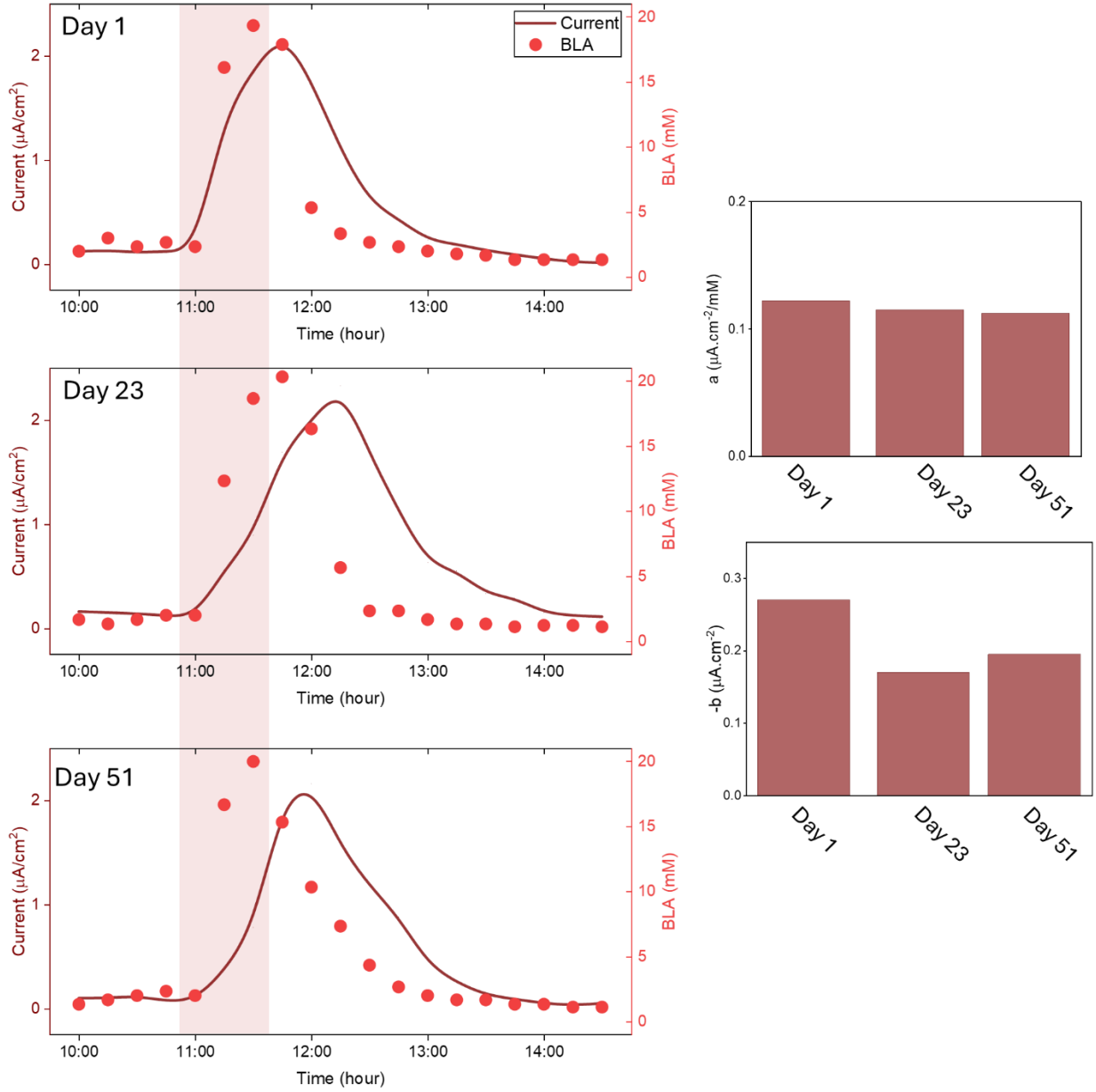
518 **Fig. S30:** Utilization of the personalized calibration protocol to convert current to  
 519 concentration in a daily test. a) Personalized coefficients values from long-term calibration  
 520 are plugged into the equation in Supplementary Note 9 to derive b)  $SBG(t)$  and  $SBHB(t)$ .

521



522

523 **Fig. S31:** Current profiles of glucose (black) and BHB (pink) from T1D subject related to  
 524 Fig.5a i and ii. Black: glucose, Pink: Ketone.



525

526 **Fig. S32:** Lactate profile of T1D subject over multiple days. Personalized coefficients  $a$   
 527 and  $b$  were evaluated on each day and their average ranged  $0.116 \frac{\mu\text{A}\cdot\text{cm}^{-2}}{\text{mM}}$  and  
 528  $-0.211 \mu\text{A}\cdot\text{cm}^{-2}$ , respectively. Red zone: Exercising timeline.

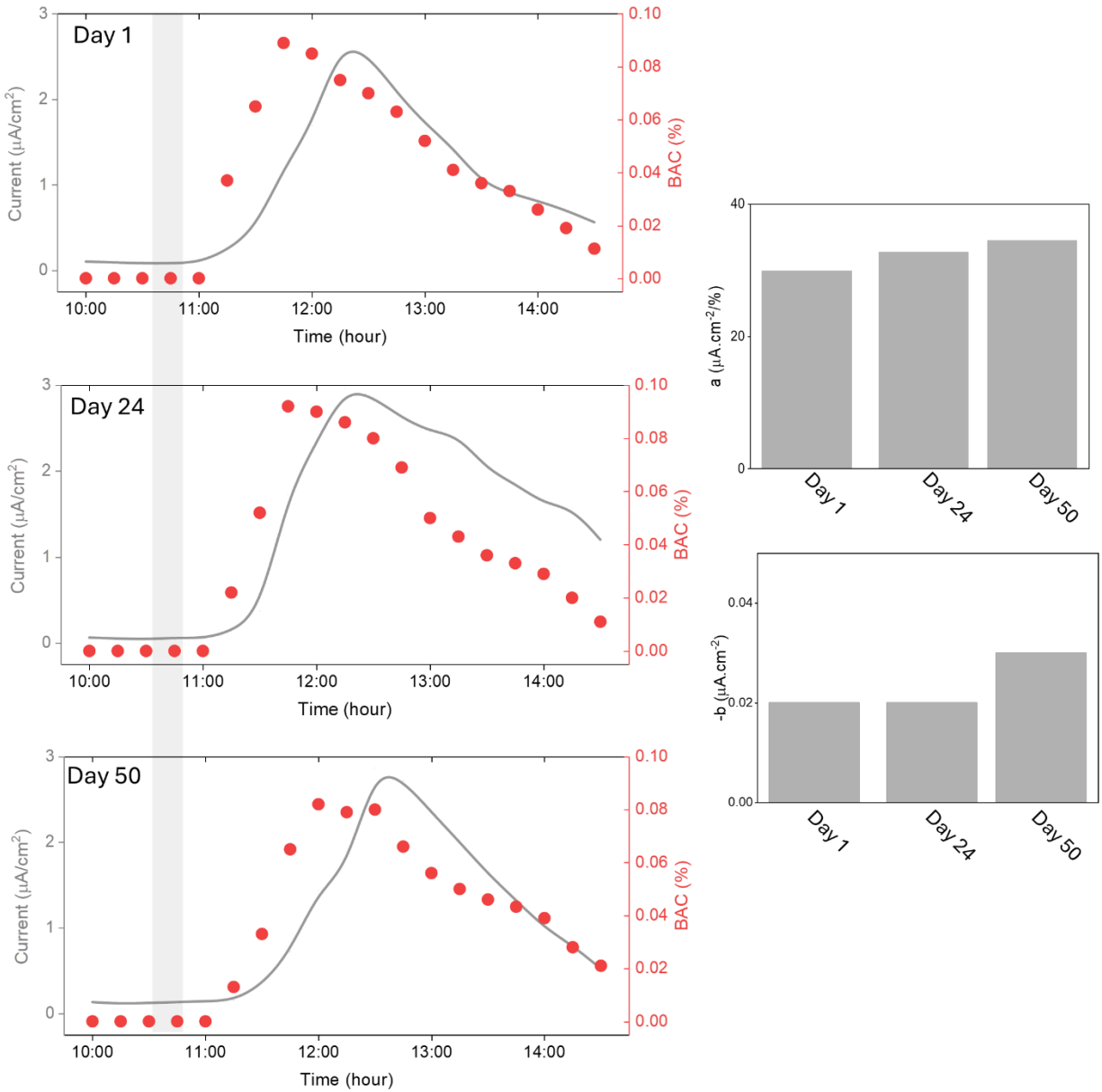
529

530

531

532

533



534

535 **Fig. S33:** Alcohol profile of T1D subject over multiple days. Personalized coefficients  $a$   
 536 and  $b$  were evaluated on each day and their average ranged  $32.38 \frac{\mu A.cm^{-2}}{\%}$  and  
 537  $-0.023 \mu A.cm^{-2}$ , respectively. Grey zone: Alcohol drink consumption timeline.

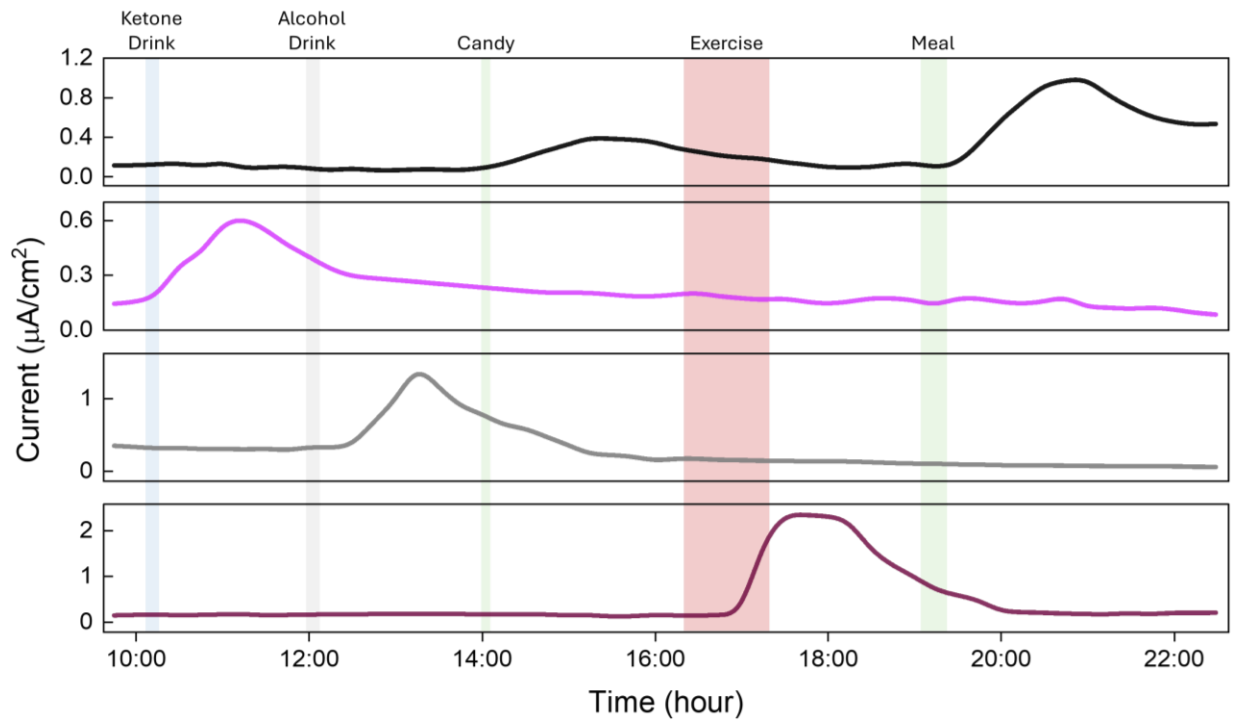
538

539

540

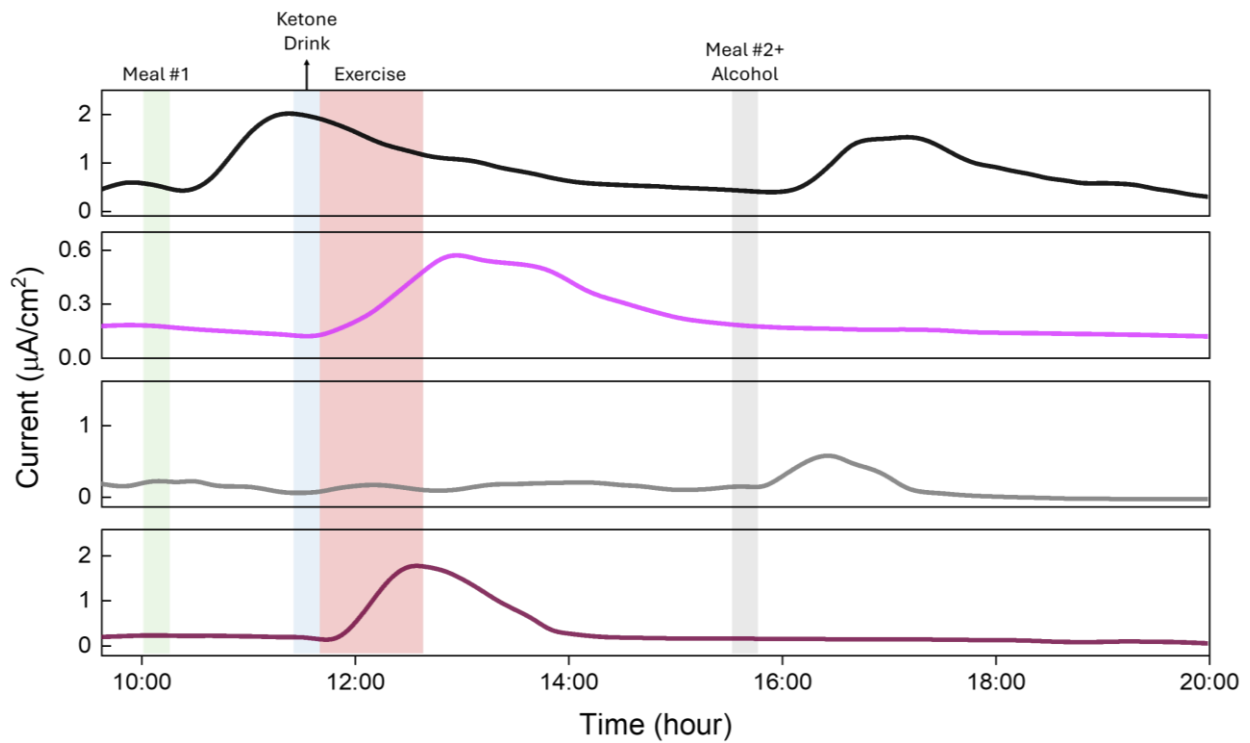
541

542



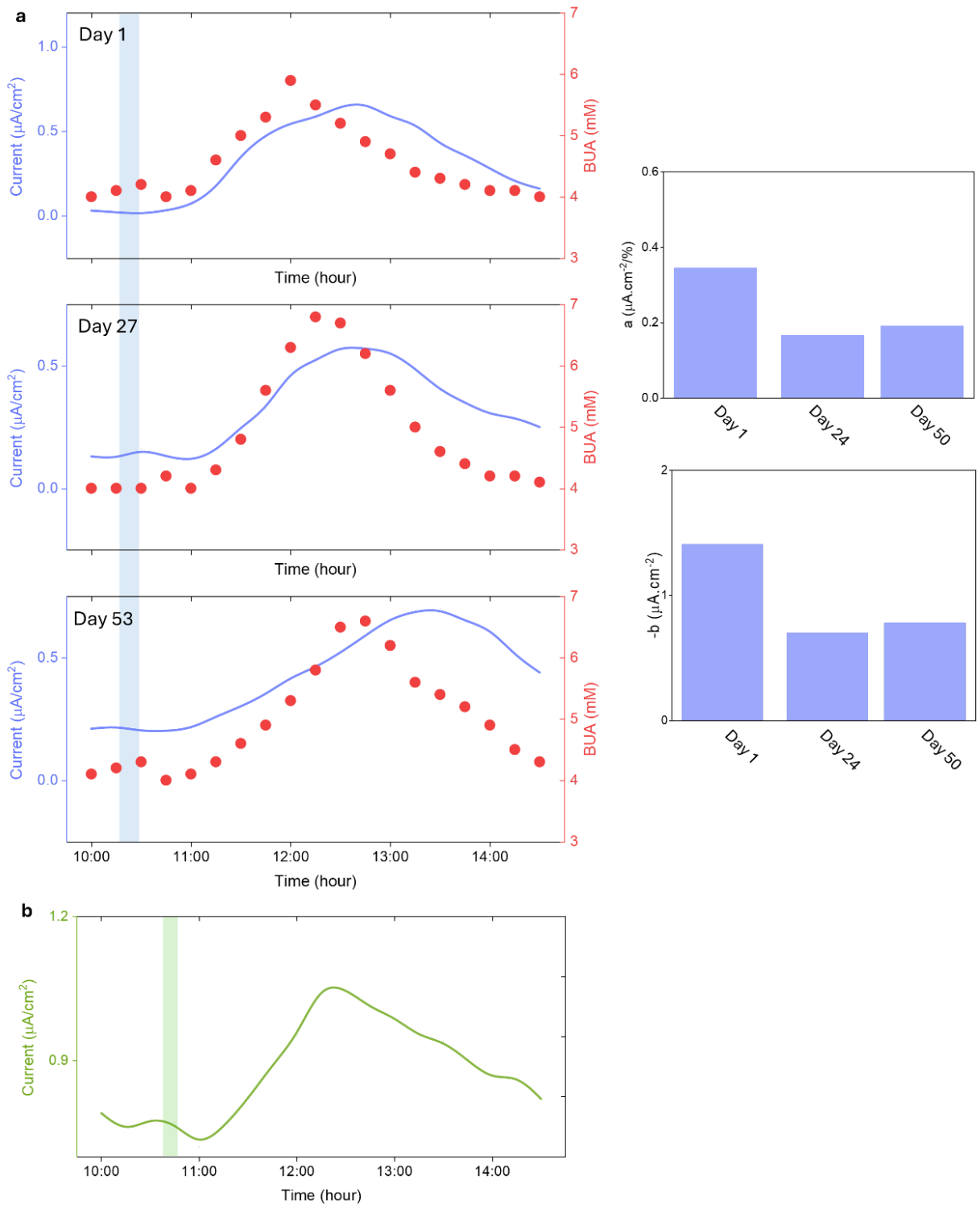
543

544 **Fig. S34:** Current profiles of glucose (black), BHB (pink), alcohol (grey) and lactate  
 545 (brown) from T1D subject related to Fig.5b.



546

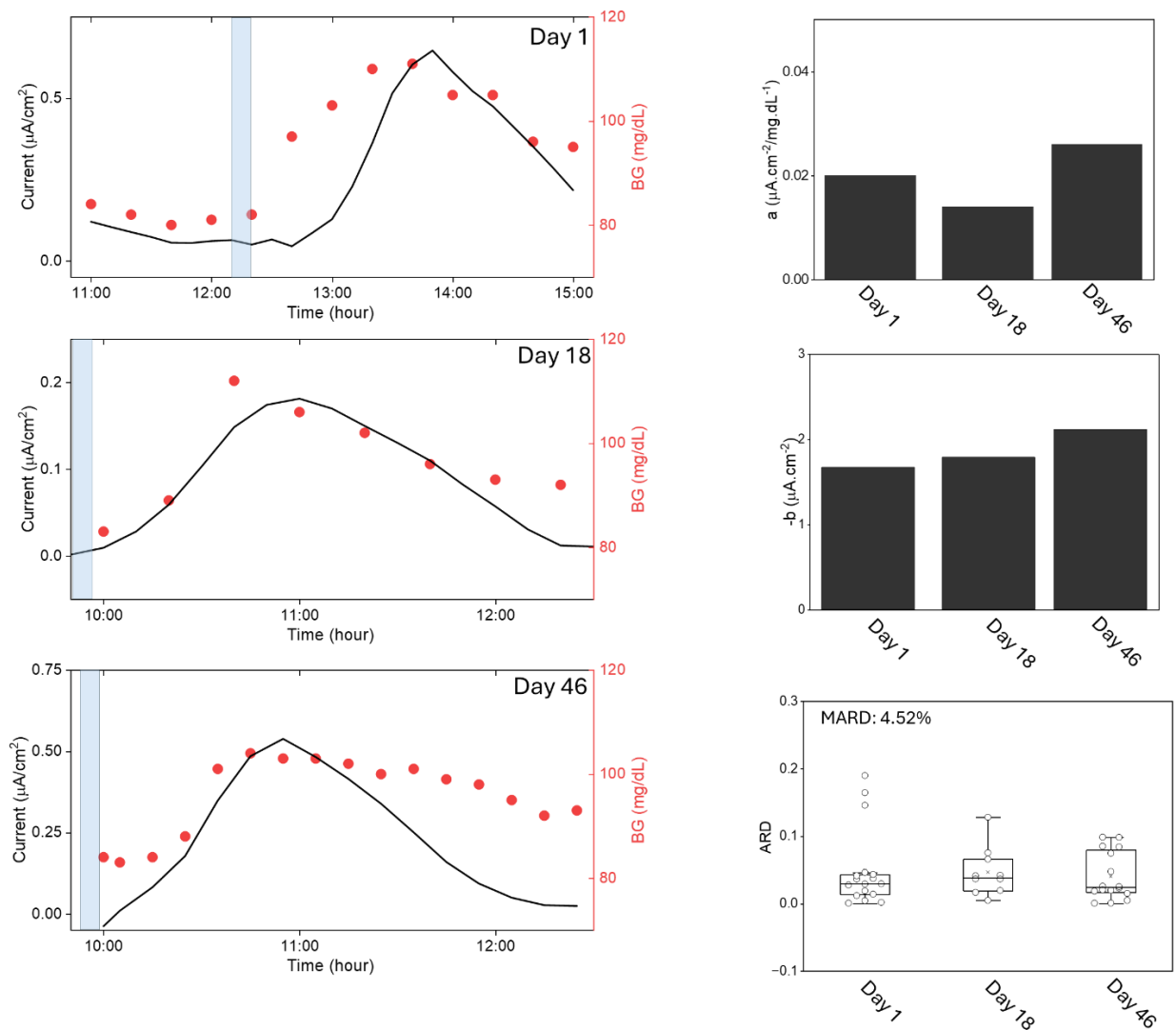
547 **Fig. S35:** Current profiles of glucose, BHB, alcohol and lactate from T1D subject related  
 548 to Fig.5c.



549

550 **Fig. S36:** UA (blue) and VC (green) profile of T1D subject over multiple days.  
 551 Personalized coefficients  $a$  and  $b$  were evaluated on each day and their average ranged  
 552  $0.235 \pm 0.097 \frac{\mu A.cm^{-2}}{mM}$  and  $-0.95 \pm 0.36 \mu A.cm^{-2}$ , respectively for UA. Blue zone: Sardine  
 553 consumption timeline. Green zone: Vit C drink consumption timeline.

554



555

556 **Fig. S37:** Glucose profile of healthy subject over multiple days. Personalized coefficients  
557  $a$  and  $b$  were evaluated on each day and their average ranged  $0.02 \frac{\mu\text{A}\cdot\text{cm}^{-2}}{\text{mg}\cdot\text{dL}^{-1}}$  and  
558  $-1.67 \mu\text{A}\cdot\text{cm}^{-2}$ , respectively. Using these values, the average MARD from three tests  
559 ranged  $\sim 4.52\%$ . Blue zone: Meal intake timeline.

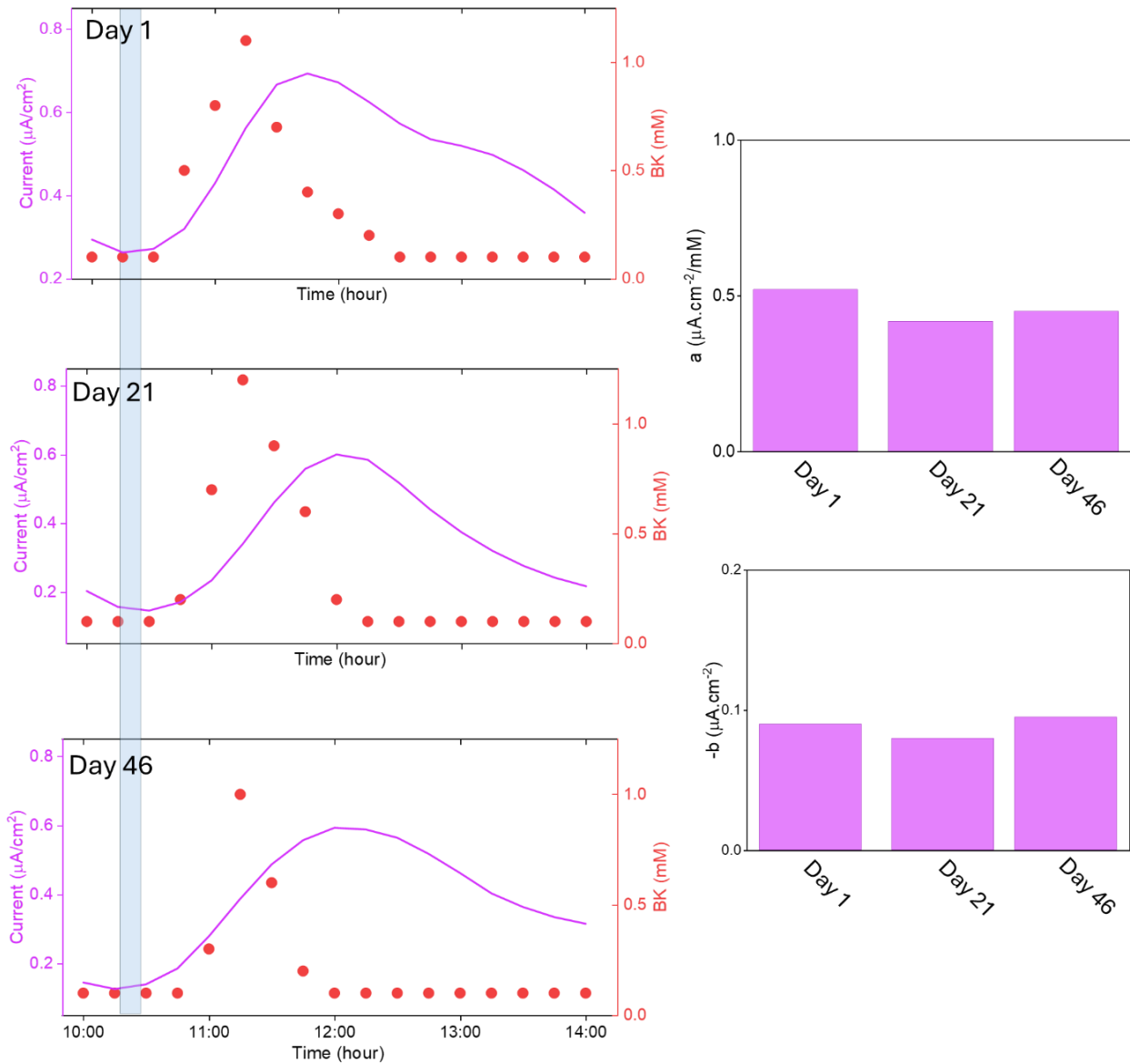
560

561

562

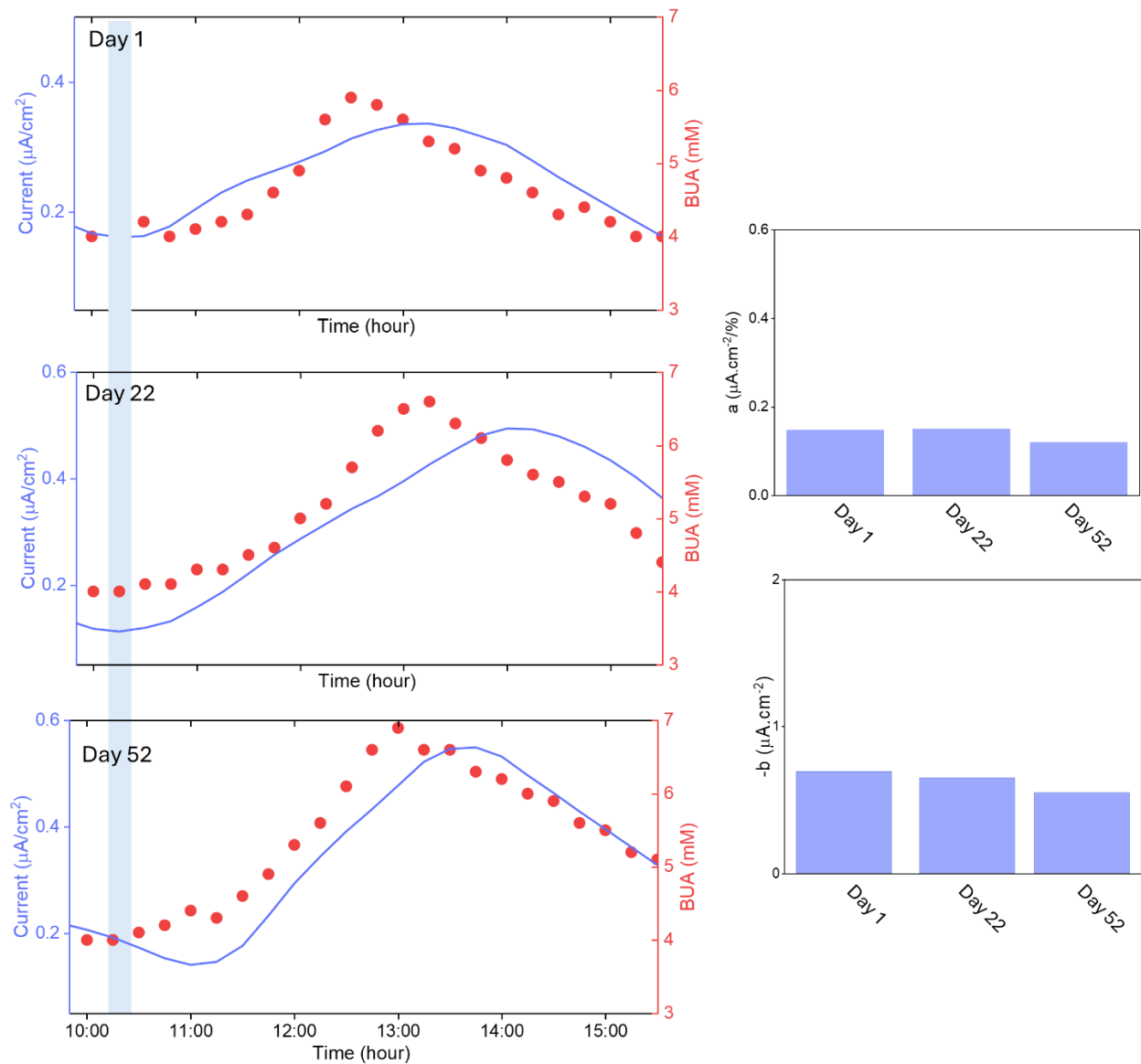
563

564



565

566 **Fig. S38:** BHB profile of healthy subject over multiple days. Personalized coefficients  $a$   
 567 and  $b$  were evaluated on each day and their average ranged  $0.46 \frac{\mu\text{A}\cdot\text{cm}^{-2}}{\text{mM}}$  and  
 568  $-0.08 \mu\text{A}\cdot\text{cm}^{-2}$ , respectively. Blue zone: BHB intake timeline.



569

570 **Fig. S39:** UA profile of healthy subject over multiple days. Personalized coefficients  $a$  and  
 571  $b$  were evaluated on each day and their average ranged  $0.13 \frac{\mu A.cm^{-2}}{mM}$  and  $-0.59 \mu A.cm^{-2}$ ,  
 572 respectively. Blue zone: Sardines intake timeline.

573

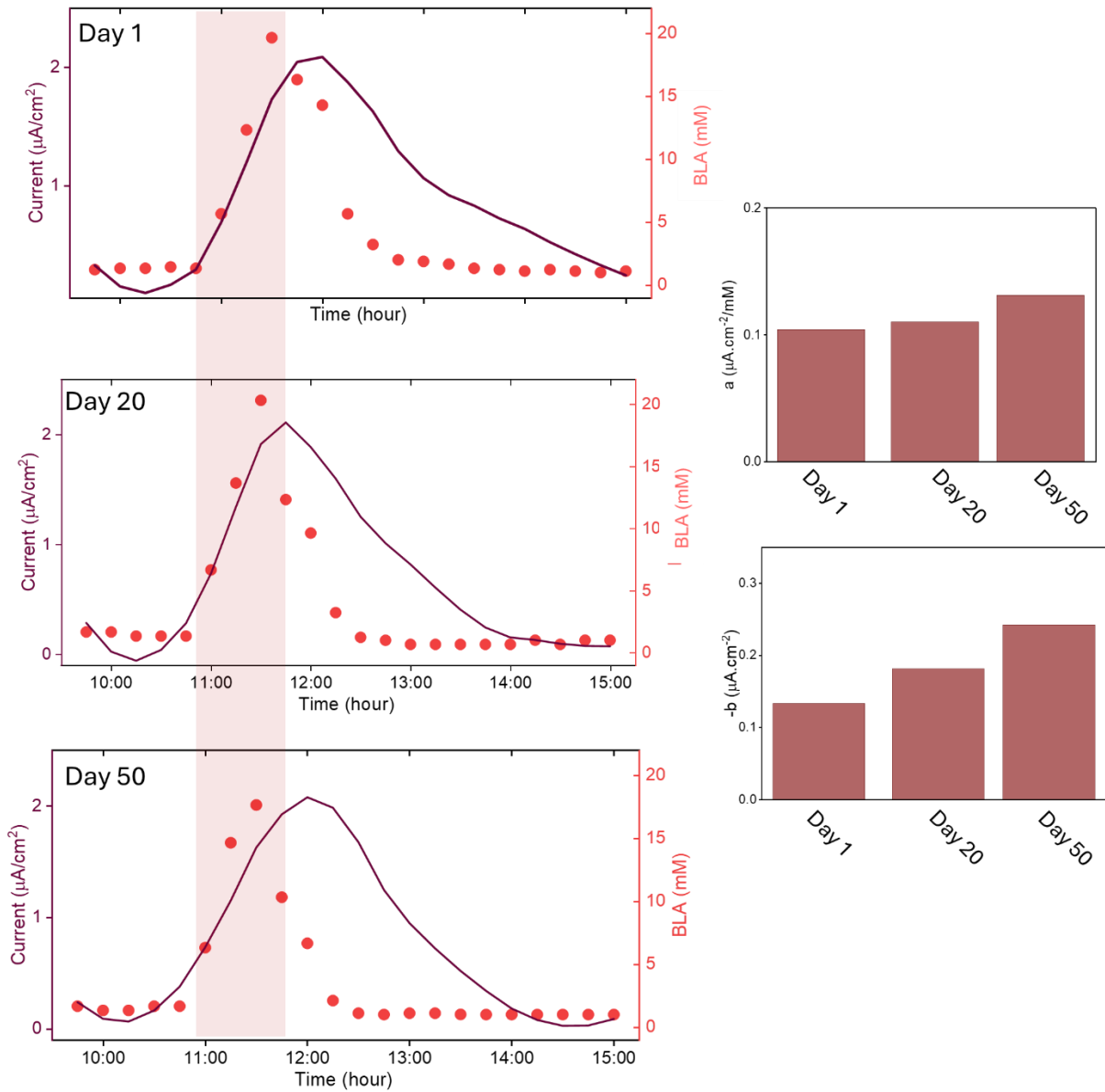
574

575

576

577

578



579

580 **Fig. S40:** Lactate profile of healthy subject over multiple days. Personalized coefficients  
 581  $a$  and  $b$  were evaluated on each day and their average ranged  $0.11 \frac{\mu\text{A}\cdot\text{cm}^{-2}}{\text{mM}}$  and  
 582  $-0.18 \mu\text{A}\cdot\text{cm}^{-2}$ , respectively. Blue zone: Exercise timeline.

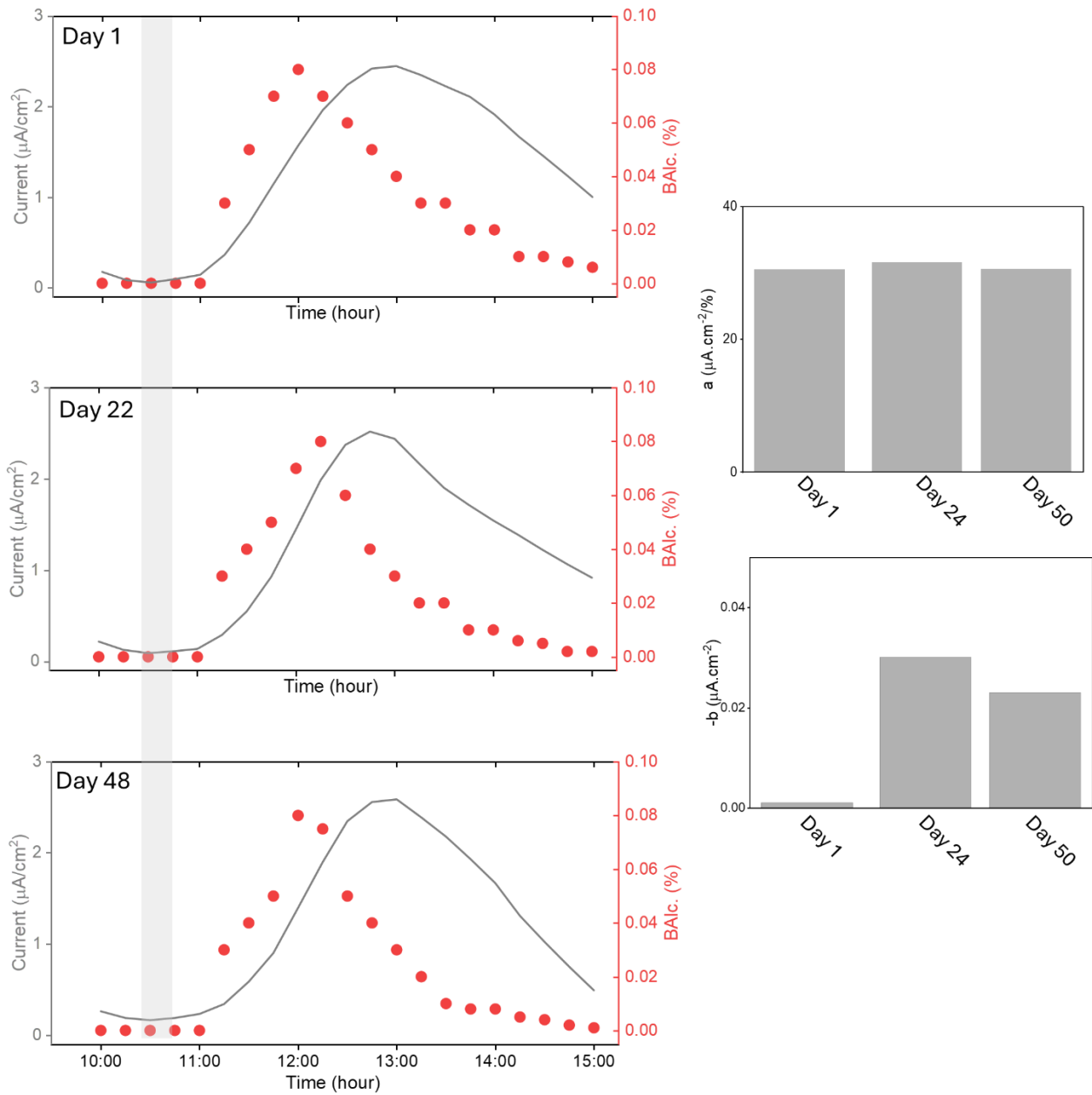
583

584

585

586

587



588

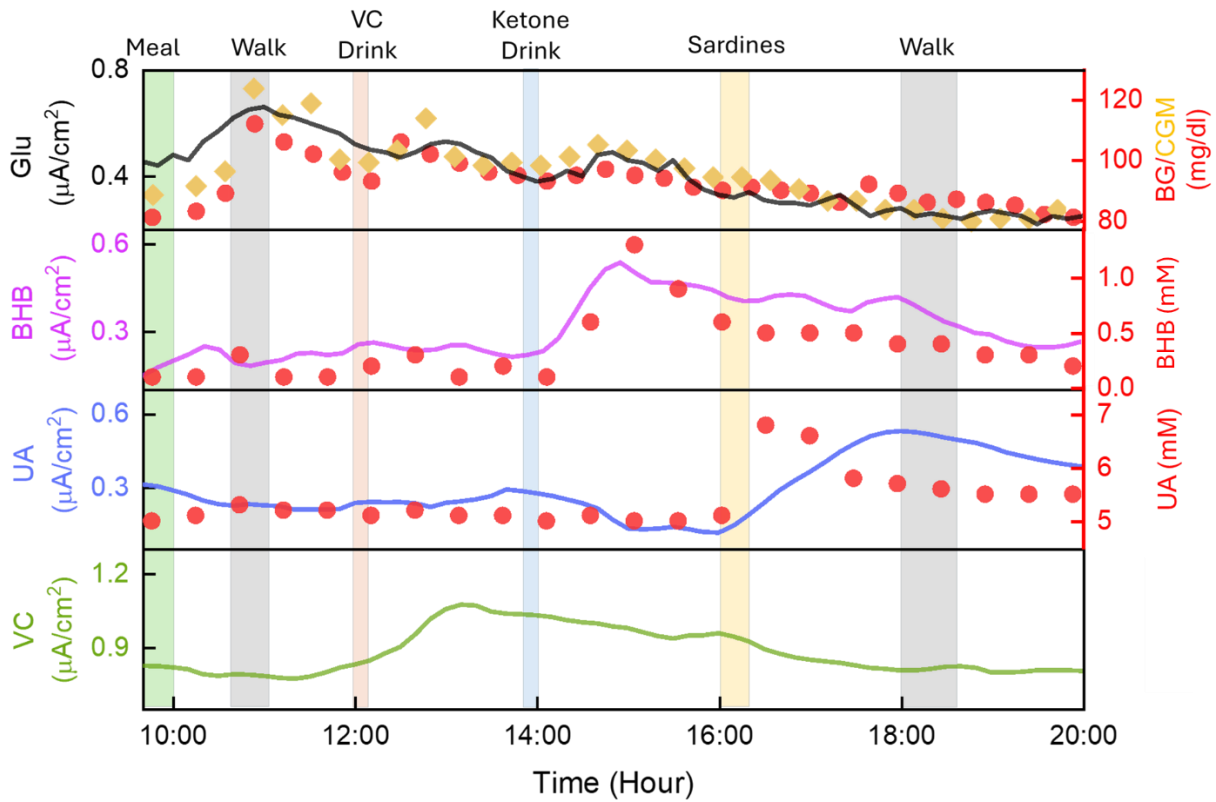
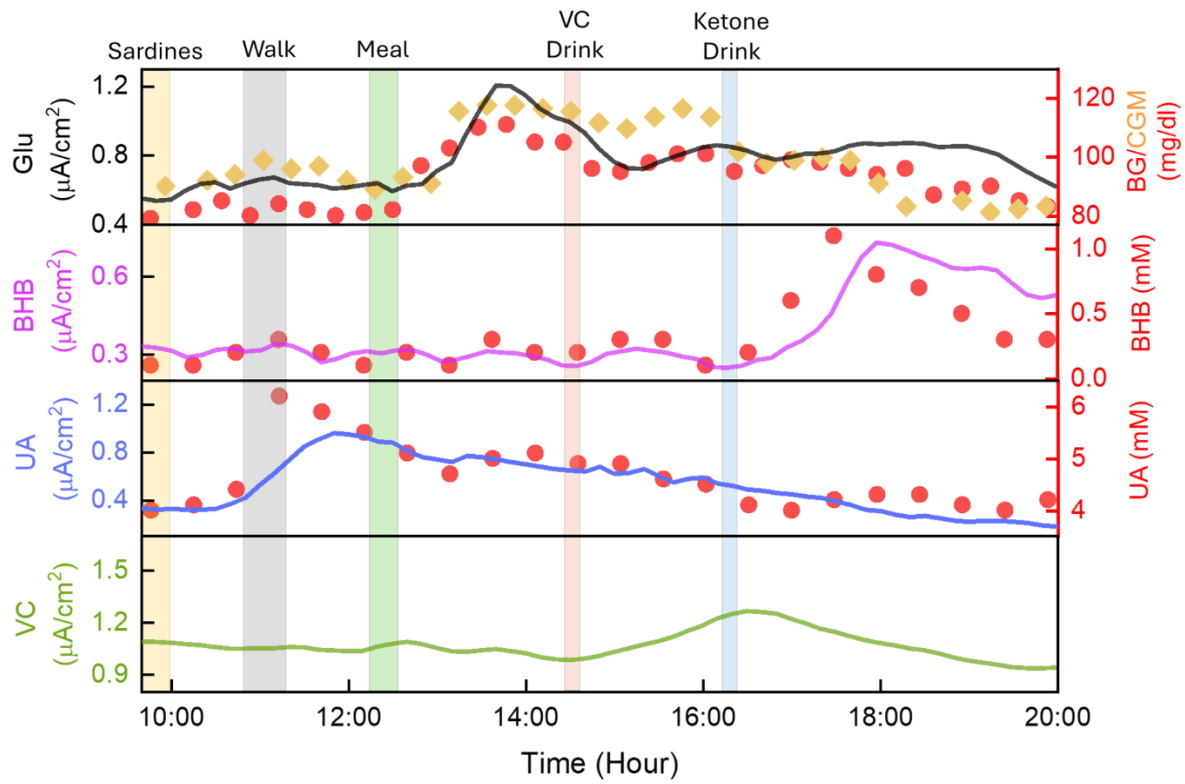
589 **Fig. S41:** Alcohol profile of healthy subject over multiple days. Personalized coefficients  
 590  $a$  and  $b$  were evaluated on each day and their average ranged  $30.73 \frac{\mu A.cm^{-2}}{\%}$  and  
 591  $-0.02 \mu A.cm^{-2}$ , respectively. Blue zone: Alcohol drink intake timeline.

592

593

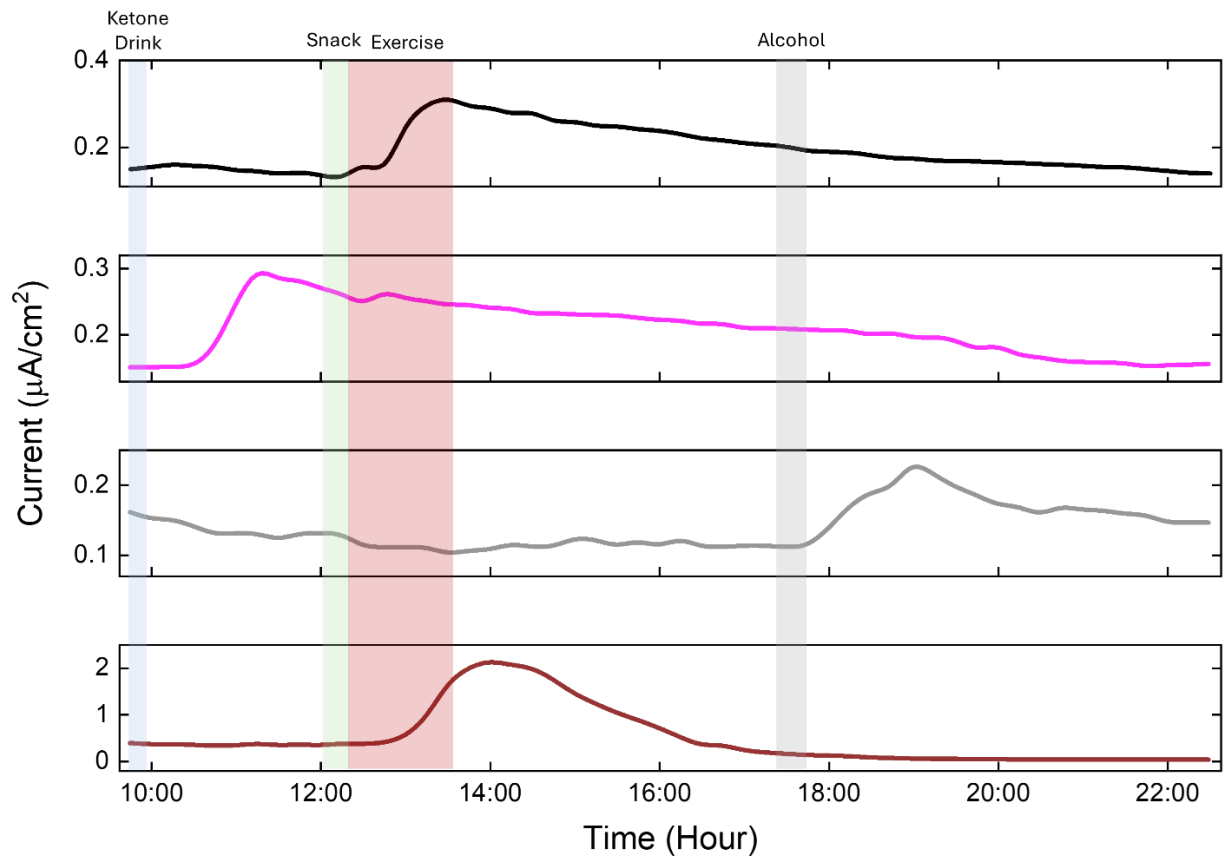
594

595



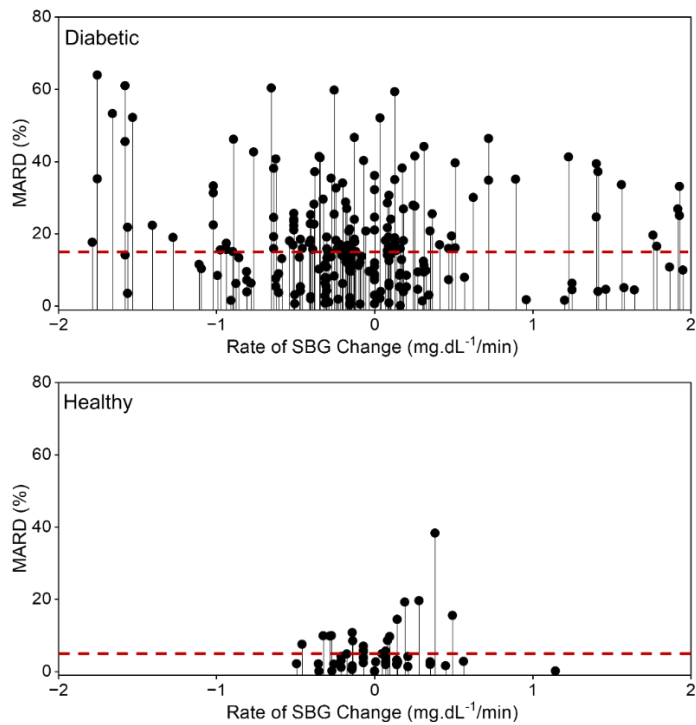
596

597 **Fig. S42:** Current profiles of glucose, AA, UA and BHB from T1D subject related to Fig.6a.



598

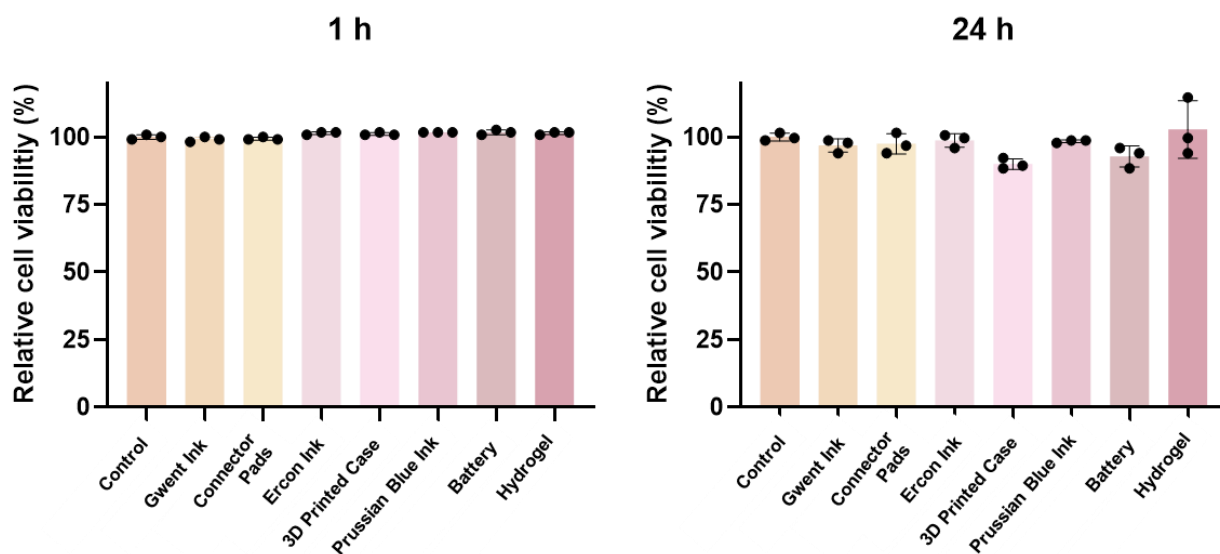
599 **Fig. S43:** Current profiles of glucose, BHB, alcohol and lactate from the healthy subject  
 600 related to Fig. 6a.



601

602 **Fig. S44:** Comparison of MARD vs. Rate of *SBG* (*t*) change. For T1-D, majority of points  
 603 with the lowest MARD lie when *SBG* change rate ranges from -1 to +0.5  $mg. dL^{-1}/min$ .  
 604 Higher MARD occurs under -1 to -2  $mg. dL^{-1}/min$  and +1 to +2  $mg. dL^{-1}/min$  range. The  
 605 average MARD (red dashed line) throughout the whole range ranges  $\sim 16.80\%$ . For  
 606 healthy, majority of points with the lowest MARD lie when *SBG* change rate ranges from  
 607 -0.5 to +0.2  $mg. dL^{-1}/min$ . Higher MARD occurs under +0.2 to +0.5  $mg. dL^{-1}/min$ . The  
 608 average MARD throughout the whole range ranges  $\sim 3.33\%$ .

609



610  
 611 **Fig. S45:** Cytotoxicity test of CHARM's components. All components achieved a viability  
 612 percentage above 90%, indicating fully safe to be used on skin.

613

614

615

616

617

618

619

620

621

622

623 **References:**

- 624 1. Razmjou, A., Liu, Q., Simon, G. P. & Wang, H. Bifunctional Polymer Hydrogel  
625 Layers As Forward Osmosis Draw Agents for Continuous Production of Fresh  
626 Water Using Solar Energy. *Environ. Sci. Technol.* **47**, 13160–13166 (2013).
- 627 2. Horkay, F., Tasaki, I. & Basser, P. J. Osmotic Swelling of Polyacrylate Hydrogels  
628 in Physiological Salt Solutions. *Biomacromolecules* **1**, 84–90 (2000).
- 629 3. Horkay, F. & Basser, P. J. Osmotic observations on chemically cross-linked DNA  
630 gels in physiological salt solutions. *Biomacromolecules* **5**, 232–237 (2004).
- 631 4. Baker, J. P., Hong, L. H., Blanch, H. W. & Prausnitz, J. M. Effect of Initial Total  
632 Monomer Concentration on the Swelling Behavior of Cationic Acrylamide-Based  
633 Hydrogels. *Macromolecules* **27**, 1446–1454 (1994).
- 634 5. Durmaz, S. & Okay, O. Acrylamide/2-acrylamido-2-methylpropane sulfonic acid  
635 sodium salt-based hydrogels: synthesis and characterization. *Polymer (Guildf)*.  
636 **41**, 3693–3704 (2000).
- 637 6. Morales, D., Palleau, E., Dickey, M. D. & Velev, O. D. Electro-actuated hydrogel  
638 walkers with dual responsive legs. *Soft Matter* **10**, 1337–1348 (2014).
- 639 7. Li, X., Qin, H., Zhang, X. & Guo, Z. Triple-network hydrogels with high strength,  
640 low friction and self-healing by chemical-physical crosslinking. *J. Colloid Interface*  
641 *Sci.* **556**, 549–556 (2019).
- 642 8. Lin, M. *et al.* A fully integrated wearable ultrasound system to monitor deep  
643 tissues in moving subjects. *Nat. Biotechnol.* **42**, 448–457 (2024).
- 644 9. Katsamanis, F. & Raftopoulos, D. D. Determination of mechanical properties of  
645 human femoral cortical bone by the Hopkinson bar stress technique. *J. Biomech.*  
646 **23**, 1173–1184 (1990).
- 647 10. Schaumburg, F., Kler, P. A. & Berli, C. L. A. Numerical prototyping of lateral flow  
648 biosensors. *Sensors Actuators, B Chem.* **259**, 1099–1107 (2018).
- 649 11. Parvazinia, M., Nassehi, V., Wakeman, R. J. & Ghoreishy, M. H. R. Finite element  
650 modelling of flow through a porous medium between two parallel plates using the  
651 Brinkman equation. *Transp. Porous Media* **63**, 71–90 (2006).
- 652 12. Dickinson, E. J. F. & Wain, A. J. The Butler-Volmer equation in electrochemical  
653 theory: Origins, value, and practical application. *J. Electroanal. Chem.* **872**,  
654 114145 (2020).

655